

The MASSIVE Survey - VIII. Stellar Velocity Dispersion Profiles and Environmental Dependence of Early-Type Galaxies

Melanie Veale,^{1,2★} Chung-Pei Ma,^{1,2★} Jenny E. Greene,³ Jens Thomas,⁴
John P. Blakeslee,⁵ Jonelle L. Walsh,⁶ Jennifer Ito¹

¹*Department of Astronomy, University of California, Berkeley, CA 94720, USA*

²*Department of Physics, University of California, Berkeley, CA 94720, USA*

³*Department of Astrophysical Sciences, Princeton University, Princeton, NJ 08544, USA*

⁴*Max Planck-Institute for Extraterrestrial Physics, Giessenbachstr. 1, D-85741 Garching, Germany*

⁵*Dominion Astrophysical Observatory, NRC Herzberg Astronomy & Astrophysics, Victoria BC V9E2E7, Canada*

⁶*George P. and Cynthia Woods Mitchell Institute for Fundamental Physics and Astronomy, and Department of Physics and Astronomy, Texas A&M University, College Station, TX 77843, USA*

Accepted XXX. Received YYY; in original form ZZZ

ABSTRACT

We measure the radial profiles of the stellar velocity dispersions, $\sigma(R)$, for 85 early-type galaxies (ETGs) in the MASSIVE survey, a volume-limited integral-field spectroscopic (IFS) galaxy survey targeting all northern-sky ETGs with absolute K -band magnitude $M_K < -25.3$ mag, or stellar mass $M_* \gtrsim 4 \times 10^{11} M_\odot$, within 108 Mpc. Our wide-field $107'' \times 107''$ IFS data cover radii as large as 40 kpc, for which we quantify separately the inner (< 5 kpc) and outer logarithmic slopes γ_{inner} and γ_{outer} of $\sigma(R)$. While γ_{inner} is mostly negative, of the 61 galaxies with sufficient radial coverage to determine γ_{outer} we find 33% to have rising outer dispersion profiles ($\gamma_{\text{outer}} \geq 0.03$), 13% to be flat ($-0.03 < \gamma_{\text{outer}} < 0.03$), and 54% to be falling. The fraction of galaxies with rising outer profiles increases with M_* and in denser galaxy environment, with the 11 most massive galaxies in our sample all having flat or rising dispersion profiles. The strongest environmental correlation is with halo mass, but weaker correlations with large-scale density and local density also exist. The average γ_{outer} is similar for brightest group galaxies, satellites, and isolated galaxies in our sample. We find a clear positive correlation between the gradients of the outer dispersion profile and the gradients of the velocity kurtosis h_4 . Altogether, our kinematic results suggest that the increasing fraction of rising dispersion profiles in the most massive ETGs are caused (at least in part) by variations in the total mass profiles rather than in the velocity anisotropy alone.

Key words: galaxies: elliptical and lenticular, cD – galaxies: evolution – galaxies: formation – galaxies: kinematics and dynamics – galaxies: structure

1 INTRODUCTION

Measuring the stellar velocity dispersion profiles of elliptical galaxies is a key ingredient of estimating their dark matter content. However, unlike spiral galaxies in which ordered rotation allows a relatively straightforward translation of rotation curves into dark matter density profiles (e.g. Rubin et al. 1980), elliptical galaxies have a complex relationship

between the gravitational potential, orbital configuration of stars, and measured line-of-sight kinematics. In addition to the measurement of dark matter, details of these relationships can also shed light on the formation and assembly history of these galaxies.

Pre-1990 long-slit measurements of the stellar velocity dispersion profiles of elliptical galaxies found most of them to decline with radius out to ~ 10 kpc (Faber et al. 1977; Tonry 1985; Wilkinson et al. 1986; Davies & Illingworth 1986; Franx et al. 1989). There are a few notable exceptions. Faber et al. (1977) found the cD galaxy in Abell 401

★ E-mail: melanie.veale@berkeley.edu (MV), cpma@berkeley.edu (C-PM)

to have a flat dispersion profile, measuring $\sigma \sim 480$ km/s at two points (in the nucleus and at ~ 43 kpc). [Davies & Illingworth \(1983\)](#) found NGC 4889 and NGC 6909 to also have flat dispersion profiles out to ~ 10 kpc. Rising dispersion profiles were rare. [Dressler \(1979\)](#) found σ for IC 1101 (BCG of Abell 29) to rise from 375 km/s at the center to 500 km/s at 70 kpc. [Carter et al. \(1981, 1985\)](#) found rising profiles for IC 2082 and the BCG of Abell 3266 (both double-nucleus galaxies) out to ~ 30 kpc, although data covering smaller radial ranges found falling or flat profiles ([Tonry 1985](#)).

Several long-slit studies since the 1990s have focused on brightest group or cluster galaxies (BGGs or BCGs), and again found mostly flat or falling dispersion profiles ([Fisher et al. 1995](#); [Sembach & Tonry 1996](#); [Carter et al. 1999](#); [Brough et al. 2007](#); [Loubser et al. 2008](#)). More than 60 galaxies were studied in these papers, but only four galaxies were found to have rising dispersion profiles. IC 1101 was confirmed as having a rising dispersion profile past at least 20 kpc ([Fisher et al. 1995](#); [Sembach & Tonry 1996](#)). [Carter et al. \(1999\)](#) found NGC 6166 to have a rising profile at ~ 20 kpc, although observations with a smaller field of view found flat or falling profiles ([Tonry 1985](#); [Loubser et al. 2008](#)). The rising profile of NGC 6166 has been confirmed in [Kelson et al. \(2002\)](#) and more recently in [Bender et al. \(2015\)](#), which found it to reach the cluster dispersion of 800 km/s at a radius of 50 kpc. This is the only study so far to confirm a smooth rise in dispersion in integrated starlight all the way to the cluster value. The dispersion profile of NGC 3311 starts to rise around 8 kpc and appears to extrapolate smoothly to the cluster dispersion ([Hau et al. 2004](#)), but the observations had a significant gap in radial coverage between the stellar dispersion and the cluster dispersion measured by galaxies. [Loubser et al. \(2008\)](#) and [Ventimiglia et al. \(2010\)](#) confirmed the rise in NGC 3311. Recently [Newman et al. \(2013\)](#) measured 7 more distant BCGs (redshifts 0.2 to 0.3) to about 30 kpc, and found all to be strikingly homogeneous in their rising dispersion profiles.

Globular cluster measurements have identified two other galaxies with rising dispersion profiles, NGC 1407 ([Pota et al. 2015](#)) and NGC 4486 (M87; [Cohen & Ryzhov 1997](#); [Côté et al. 2001](#); [Wu & Tremaine 2006](#)). In the case of NGC 4486, [Sembach & Tonry \(1996\)](#) found a falling profile, but [Murphy et al. \(2011, 2014\)](#) confirmed the rise in σ at large radius.

Several past and ongoing IFU surveys produce 2-dimensional maps of stellar kinematics for large samples of galaxies and provide an even more comprehensive picture of velocity dispersion profiles than long-slit observations. The ATLAS^{3D} survey ([Emsellem et al. 2011](#)) measured stellar kinematics to between $0.5R_e$ and $1R_e$ for a large sample of ETGs. Data beyond $1R_e$, however, are needed to study the outer behaviour of the dispersion profiles. The SLUGGS survey mapped the kinematics out to $\sim 3R_e$ for 25 ATLAS^{3D} galaxies ([Brodie et al. 2014](#); [Arnold et al. 2014](#)). No dispersion profiles of these galaxies have been quantified thus far, but our visual inspections of their $\sigma(R)$ plots found only flat or falling dispersion profiles ([Foster et al. 2016](#)). [Raskutti et al. \(2014\)](#) measured kinematics to a few R_e for 33 ETGs and found flat or declining dispersion profiles past $1R_e$, with only the two most massive galaxies showing small increases in dispersion outside $1R_e$. The ongoing SAMI survey probes to between $1R_e$ and $2R_e$ ([van de Sande et al. 2017](#)) and may

be more likely to provide statistics of the outer dispersion profiles.

A rising dispersion profile is generally interpreted as evidence for an increasing dynamical mass-to-light ratio, but velocity anisotropy can complicate the interpretations ([Binney & Mamon 1982](#)). Information about the full shape of the line-of-sight velocity distributions (LOSVD), in particular at least the kurtosis h_4 , is needed to determine both the mass and the anisotropy ([Dejonghe & Merritt 1992](#); [Merritt & Saha 1993](#); [Gerhard 1993](#)). Gravitational lensing data often favor roughly isothermal mass profiles for ETGs ([Treu et al. 2006](#); [Koopmans et al. 2009](#); [Auger et al. 2009, 2010](#); [Sonnenfeld et al. 2013](#)). There is also some evidence that mass profiles depend on galaxy mass ([Deason et al. 2012](#); [Newman et al. 2013](#); [Alabi et al. 2016](#)) or environment ([Newman et al. 2015](#)), with steeper profiles at lower mass and density and shallower profiles at higher mass and density. If mass profiles change, then dispersion profiles are also likely to change with galaxy mass or environment. In addition, the anisotropy of a galaxy may be linked to its merger history ([Romanowsky et al. 2003](#)), which in turn links to galaxy mass and environment, and dispersion profiles may be directly impacted by recent mergers ([Schauer et al. 2014](#)).

In this paper we present the stellar velocity dispersion profiles, $\sigma(R)$, of 85 massive early-type galaxies in the volume-limited MASSIVE survey ([Ma et al. 2014](#); Paper I). We measure the inner and outer gradients of $\sigma(R)$ and quantify how they correlate with galaxy mass, environment, and velocity kurtosis h_4 . The MASSIVE survey uses the wide-format ($107'' \times 107''$) Mitchell/VIRUS-P IFS to obtain 2-D kinematic maps out to radii as large as 40 kpc for the most massive local ETGs. The survey is designed with clean sample selection criteria, targeting all ETGs with stellar mass $M_* \gtrsim 4 \times 10^{11} M_\odot$ within 108 Mpc in the northern sky, regardless of galaxy environment, size, dispersion, or other properties. Details of our IFS data and kinematic analysis were described in [Veale et al. \(2017a\)](#) (Paper V). A study of the relationship between MASSIVE galaxy rotation, stellar mass, and four measures of galaxy environments (group membership, halo mass M_{halo} , large-scale galaxy density δ_g , and local galaxy density ν_{10}) was presented in [Veale et al. \(2017b\)](#) (Paper VII). This paper continues the stellar kinematic study of MASSIVE galaxies and focuses on the radial profiles of the stellar velocity dispersions.

Other results from the MASSIVE survey were discussed in separate papers: stellar population gradients ([Greene et al. 2015](#); Paper II), molecular gas content and kinematics ([Davis et al. 2016](#); Paper III), X-ray halo gas properties ([Goulding et al. 2016](#); Paper IV), spatial distributions and kinematics of warm ionized gas ([Pandya et al. 2017](#); Paper VI), and measurement of the black hole mass in MASSIVE galaxy NGC 1600 ([Thomas et al. 2016](#)).

Section 2 of this paper summarizes our sample of galaxies and our earlier kinematic and environmental analyses. Section 3 describes how we quantify $\sigma(R)$ and presents our results for the inner and outer power law slopes γ_{inner} and γ_{outer} of $\sigma(R)$. Section 4 examines the relationships of the dispersion profiles and the higher moment h_4 , the kurtosis of the stellar velocity distribution, and Section 5 examines how the dispersion profiles relate to galaxy mass and environment. Section 6 summarizes the results and possible implications. The velocity dispersion profiles for all 85 galaxies

are shown in [Appendix A](#), along with a discussion of special individual cases.

2 GALAXY SAMPLE, PROPERTIES, AND ENVIRONMENT

The MASSIVE survey targets a volume-limited sample of 116 early-type galaxies (ETGs) in the northern hemisphere and away from the galactic plane,¹ with stellar masses $M_* > 4 \times 10^{11} M_\odot$ (estimated from K -band magnitudes $M_K < -25.3$ mag) and distances $D < 108$ Mpc. The galaxies were selected from the Extended Source Catalogue (XSC; [Jarrett et al. 2000](#)) of the Two Micron All Sky Survey (2MASS; [Skrutskie et al. 2006](#)). The sample selection, methodology, and science goals of the survey were described in [Ma et al. \(2014\)](#) (Paper I of the MASSIVE survey). Uncertainties in galaxy parameters such as D , M_K , M_* , and R_e were discussed in [Ma et al. \(2014\)](#) and [Veale et al. \(2017a,b\)](#).

Thus far we have observed 85 MASSIVE galaxies with the Mitchell/VIRUS-P Integral Field Spectrograph (IFS) at the McDonald Observatory ([Hill et al. 2008](#)). This IFS covers a large $107'' \times 107''$ field of view with 246 evenly-spaced $4''$ -diameter fibres and a one-third filling factor, which we use to obtain contiguous coverage by observing each galaxy with three dither positions. The spectral range of the IFS spans 3650\AA to 5850\AA , covering the Ca H+K region, the G-band region, $H\beta$, the Mgb region, and many Fe absorption features. The instrumental resolution varies by factors of about 20 per cent over this wavelength range but is typically around 4.5\AA full width at half-maximum.

The spectra from individual fibres in the central regions of our galaxies typically have a signal-to-noise ratio (S/N) exceeding 50, and we use these single-fibre spectra directly in the kinematic analysis. Beyond the central regions, we combine the fibres with lower S/N into radial and azimuthal bins, folding across the major axis and combining symmetrical bins such that each resulting co-added spectrum reaches at least $S/N = 20$. The line-of-sight velocity distribution (LOSVD) is parametrized as a Gauss-Hermite series up to order 6, and we obtain the best-fitting velocity V , dispersion σ , and higher order moments h_3 , h_4 , h_5 , and h_6 using the penalized pixel-fitting (pPXF) method of [Cappellari & Emsellem \(2004\)](#). Details of our kinematic analysis such as spectral continuum modeling, stellar template fitting, and error determination were described in [Veale et al. \(2017a\)](#) (Paper V).

Our results for four measures of galaxy environments – group membership, halo mass M_{halo} , large-scale galaxy density δ_g , and local galaxy density ν_{10} – were presented in [Veale et al. \(2017b\)](#) (Paper VII) and listed in Table 1. Briefly, we take group membership and halo mass information from the HDC catalogue of [Crook et al. \(2007, 2008\)](#), which is based on the 2MRS sample of [Huchra et al. \(2005a,b\)](#). Based on whether a galaxy is in a group with at least 3 members in the HDC catalogue, we assign each of our galaxies to be “Isolated”, a “Satellite” galaxy in a group, or “Brightest Group Galaxy” (BGG). We use M_{halo} measured by the projected

mass estimator ([Heisler et al. 1985](#)) from the HDC catalogue; the 15 isolated galaxies in our sample therefore do not have a halo mass estimate. For the well-studied clusters of Virgo, Coma, and Perseus, we replace the M_{halo} taken from the HDC catalogue with values from the literature: $M_{\text{halo}} = 5.5 \times 10^{14} M_\odot$ for Virgo ([Durrell et al. 2014; Ferrarese et al. 2012; Schindler et al. 1999](#)), $M_{\text{halo}} = 1.8 \times 10^{15} M_\odot$ for Coma ([Kubo et al. 2007; Falco et al. 2014; Rines et al. 2003](#)), and $M_{\text{halo}} = 6.7 \times 10^{14} M_\odot$ for Perseus. The luminosity-weighted large-scale density contrast δ_g is calculated with a smoothing scale of a few Mpc in [Carrick et al. \(2015\)](#) based on the 2M++ redshift catalogue of [Lavaux & Hudson \(2011\)](#). We define the local density ν_{10} as the luminosity density within a sphere out to the 10th nearest neighbour of the galaxy; see Section 3.4 and Appendix A of [Veale et al. \(2017b\)](#) for details.

3 RADIAL PROFILES OF STELLAR VELOCITY DISPERSION

3.1 Quantifying $\sigma(R)$

The radial profiles of the stellar velocity dispersion, $\sigma(R)$, for the 85 MASSIVE galaxies are shown in [Figure 1](#) in three increasing M_* bins. As M_* increases (from left to right panels), the overall amplitude of σ increases, and more σ profiles become flat or rising in the outer parts instead of falling monotonically. [Figure 2](#) illustrates three types of $\sigma(R)$ shapes that we have found for MASSIVE galaxies: falling monotonically with R (left), a “U” shape that falls to a minimum before rising at larger R (middle), and rising monotonically with R (right). Some galaxies are consistent with a flat $\sigma(R)$, but we find no galaxies that convincingly show $\sigma(R)$ with an upside-down “U” shape that rises to a maximum and falls at large radius.

To quantify the overall shape of $\sigma(R)$, we fit a broken power law form as in [Veale et al. \(2017a\)](#):

$$\sigma(R) = \sigma_0 2^{\gamma_1 - \gamma_2} \left(\frac{R}{R_b} \right)^{\gamma_1} \left(1 + \frac{R}{R_b} \right)^{\gamma_2 - \gamma_1}, \quad (1)$$

where the break radius R_b is fixed at 5 kpc. Although the apparent break radius varies somewhat below and above this value among different galaxies, degeneracies among R_b , γ_1 , and γ_2 allow as good a fit for every galaxy with this fixed R_b as with a free R_b . We find 64 of the 85 galaxies to be well fit by a single power law ($\gamma_1 \equiv \gamma_2$). The rest of the sample shows distinct inner and outer slopes, meaning that the fit improves substantially by allowing $\gamma_1 \neq \gamma_2$. Example fits are shown in [Figure 2](#), and fits for all 85 galaxies are shown in [Appendix A](#) with a description of special individual cases. Allowing $\gamma_1 > \gamma_2$ provides only marginal improvement to the fits, so we exclude that portion of the parameter space.

The parameters γ_1 and γ_2 in [Equation 1](#) represent the asymptotic logarithmic slopes of $\sigma(R)$, whose values can be more extreme than the slopes of $\sigma(R)$ in the radial range covered by our IFS data. To account for this, we convert γ_1 and γ_2 to the *local* logarithmic slopes γ_{inner} and γ_{outer} , where γ_{inner} is the power law slope that passes through the fit at 1 and 2 kpc, and γ_{outer} is the power law slope of the fit in the outermost 20% of the data points.

[Table 1](#) lists our measurements of γ_{inner} for all 85 MASSIVE galaxies and γ_{outer} for 61 galaxies for which our IFS

¹ The total is 115 galaxies after we remove NGC 7681, which our IFS data revealed as a close pair of less-luminous bulges ([Veale et al. 2017a](#)), each below the magnitude cut of our survey.

Table 1. Properties of MASSIVE galaxies

Galaxy	M_K [mag]	$\log_{10} M_*$ [M_\odot]	λ_e	σ_c [km/s]	$\langle\sigma\rangle_e$ [km/s]	γ_{inner}	γ_{outer}	$\langle h_4 \rangle$	h'_4	env	$\log_{10} M_{\text{halo}}$ [M_\odot]	$1 + \delta_g$	v_{10} [\bar{v}]
(1)	(2)	(3)	(4)	(5)	(6)	(7)	(8)	(9)	(10)	(11)	(12)	(13)	(14)
NGC 0057	-25.75	11.79	0.02	289	251	-0.110	-0.110	0.053	0.017	I		2.29	4.8
NGC 0080	-25.66	11.75	0.04	248	222	-0.083	0.106	0.039	0.010	B	14.1	2.95	6500
NGC 0315	-26.30	12.03	0.06	348	341	-0.022	-0.022	0.052	0.011	B	13.5	6.03	270
NGC 0383	-25.81	11.82	0.25	290	257	-0.097	0.129	0.012	-0.019	S	14.4	7.24	4300
NGC 0410	-25.90	11.86	0.03	291	247	-0.128	-0.128	0.041	-0.028	B	14.4	7.41	3100
NGC 0499	-25.50	11.68	0.06	274	266	-0.196	-0.196	0.028	-0.008	S	14.4	7.24	35000
NGC 0507	-25.93	11.87	0.05	274	257	-0.071	0.057	0.050	0.035	B	14.4	7.24	58000
NGC 0533	-26.05	11.92	0.03	280	258	-0.063	0.047	0.063	0.083	B	13.5	4.27	13
NGC 0545	-25.83	11.83	0.13	249	231	-0.007	-0.007	0.074	0.036	B(A194)	14.5	5.89	13000
NGC 0547	-25.83	11.83	0.06	259	232	-0.064	-0.064	0.035	0.030	S(A194)	14.5	5.89	14000
NGC 0665	-25.51	11.68	0.40	206	164	-0.152	-0.152	-0.074	-0.227	B	13.7	3.02	56
UGC 01332	-25.57	11.71	0.04	248	253	0.030		0.034	-0.020	B	13.8	3.72	170
NGC 0708	-25.65	11.75	0.04	206	219	-0.028	0.209	0.090	0.110	B(A262)	14.5	5.75	12000
NGC 0741	-26.06	11.93	0.04	292	289	0.012		0.043	0.069	B	13.8	2.88	130
NGC 0777	-25.94	11.87	0.05	324	291	-0.111		0.051	0.004	B	13.5	5.01	76
NGC 0890	-25.50	11.68	0.10	207	194	-0.035		-0.006	-0.002	I		4.68	1.4
NGC 0910	-25.33	11.61	0.04	236	219	-0.227	0.278	0.018	0.034	S(A347)	14.8	6.17	11000
NGC 0997	-25.40	11.64	0.24	267	215	-0.169		0.021	-0.015	B	13.0	2.95	26
NGC 1016	-26.33	12.05	0.03	286	279	-0.020	-0.020	0.027	-0.001	B	13.9	4.79	55
NGC 1060	-26.00	11.90	0.02	310	271	-0.086		0.055	0.028	B	14.0	3.89	2000
NGC 1132	-25.70	11.77	0.06	239	218	-0.087	0.096	0.022	0.015	B	13.6	3.39	8.1
NGC 1129	-26.14	11.96	0.12	241	259	0.023	0.127	0.047	0.043	B	14.8	10.72	16000
NGC 1167	-25.64	11.74	0.43	188	172	-0.126	-0.126	-0.068	-0.166	B	13.1	5.01	15
NGC 1226	-25.51	11.68	0.03	274	229	-0.116	-0.116	0.084	0.138	B	13.2	3.47	3.0
IC0 310	-25.35	11.61	0.09	218	205	-0.262	-0.262	0.059	-0.074	S(Perseus)	14.8	13.18	15000
NGC 1272	-25.80	11.81	0.02	285	250	-0.042	-0.042	0.049	0.046	S(Perseus)	14.8	13.49	390000
UGC 02783	-25.44	11.65	0.07	292	266	-0.133		0.018	0.015	B	12.6	6.31	17
NGC 1453	-25.67	11.75	0.20	312	272	-0.042	-0.042	0.044	0.005	B	13.9	2.29	87
NGC 1497	-25.31	11.60	0.47	234	190	-0.103	-0.103	-0.029	-0.071	I		2.69	87
NGC 1600	-25.99	11.90	0.03	346	293	-0.063	-0.063	0.055	0.037	B	14.2	6.03	1200
NGC 1573	-25.55	11.70	0.04	288	264	-0.066	-0.066	0.018	0.015	B	14.1	4.07	580
NGC 1684	-25.34	11.61	0.12	295	262	-0.078	-0.078	0.018	0.011	B	13.7	6.17	1500
NGC 1700	-25.60	11.72	0.20	236	223	-0.152	-0.152	-0.026	-0.074	B	12.7	3.47	23
NGC 2208	-25.63	11.74	0.06	268	255	-0.013		-0.004	-0.007	I		2.82	7.1
NGC 2256	-25.87	11.84	0.02	240	259	0.049		0.063	0.004	B	13.7	2.69	20
NGC 2274	-25.69	11.76	0.07	288	259	-0.081	0.059	0.021	-0.024	B	13.3	3.09	110
NGC 2258	-25.66	11.75	0.04	293	254	-0.072		0.040	0.042	B	12.2	3.80	9.5
NGC 2320	-25.93	11.87	0.23	340	298	-0.122		0.037	0.028	B	14.2	7.94	650
UGC 03683	-25.52	11.69	0.09	257	257	-0.055		0.024	-0.090	B	13.6	5.75	26
NGC 2340	-25.90	11.86	0.03	232	235	-0.008	-0.008	0.018	0.004	S	14.2	7.76	1200
UGC 03894	-25.58	11.72	0.12	297	255	-0.122	-0.122	0.036	0.025	B	13.7	1.55	1.5
NGC 2513	-25.52	11.69	0.10	280	253	-0.071	-0.071	-0.004	-0.025	B	13.6	2.34	5.1
NGC 2672	-25.60	11.72	0.10	273	262	-0.047		0.028	-0.009	B	13.0	1.32	1.2
NGC 2693	-25.76	11.79	0.29	327	296	-0.041	-0.041	0.035	-0.011	I		1.70	6.8
NGC 2783	-25.72	11.78	0.04	252	264	0.026	0.026	0.047	-0.007	B	12.8	3.24	4.6
NGC 2832	-26.42	12.08	0.07	327	291	-0.074	0.073	0.054	0.005	B(A779)	13.7	3.98	7.8
NGC 2892	-25.70	11.77	0.05	237	234	-0.038	-0.038	0.051	0.004	I		2.19	2.2
NGC 3158	-26.28	12.02	0.26	301	289	-0.017	-0.017	0.032	0.009	B	13.3	2.69	9.5
NGC 3209	-25.55	11.70	0.04	288	247	-0.099		0.005	-0.025	B	11.8	2.40	2.7
NGC 3462	-25.62	11.73	0.09	233	214	-0.072	-0.072	-0.017	-0.015	I		2.24	2.5
NGC 3562	-25.65	11.75	0.04	250	241	-0.072	-0.072	0.028	-0.021	B	13.5	2.24	8.3
NGC 3615	-25.58	11.72	0.40	268	232	-0.090	-0.090	-0.030	-0.044	B	13.6	3.09	5.1
NGC 3805	-25.69	11.76	0.50	266	225	-0.223	-0.031	0.019	-0.060	S(A1367)	14.8	5.62	430
NGC 3842	-25.91	11.86	0.04	262	231	-0.037		0.022	-0.000	B(A1367)	14.8	5.89	18000
NGC 3862	-25.50	11.68	0.06	247	232	-0.012	-0.012	-0.050	-0.175	S(A1367)	14.8	5.89	18000
NGC 3937	-25.62	11.73	0.07	292	243	-0.082		0.015	-0.002	B	14.2	5.89	69
NGC 4073	-26.33	12.05	0.02	316	292	-0.065	0.106	0.034	0.043	B	13.9	4.37	87
NGC 4472	-25.72	11.78	0.20	292	258	-0.064		0.023	0.020	B(Virgo)	14.7	8.91	1800
NGC 4555	-25.92	11.86	0.12	328	277	-0.129	-0.129	0.044	0.022	I		5.89	6.2
NGC 4839	-25.85	11.83	0.05	261	275	0.036		0.061	0.099	S(Coma)	15.3	13.18	2600
NGC 4874	-26.18	11.98	0.07	251	258	-0.061	0.278	0.046	0.051	S(Coma)	15.3	13.18	23000

Table 1 – continued

Galaxy	M_K [mag]	$\log_{10} M_*$ [M_\odot]	λ_e	σ_c [km/s]	$\langle \sigma \rangle_e$ [km/s]	γ_{inner}	γ_{outer}	$\langle h_4 \rangle$	h'_4	env	$\log_{10} M_{\text{halo}}$ [M_\odot]	$1 + \delta_g$	ν_{10} [$\bar{\nu}$]
(1)	(2)	(3)	(4)	(5)	(6)	(7)	(8)	(9)	(10)	(11)	(12)	(13)	(14)
NGC 4889	-26.64	12.18	0.03	370	337	-0.105	0.072	0.051	0.055	B(Coma)	15.3	13.18	18000
NGC 4914	-25.72	11.78	0.05	233	225	-0.029	-0.029	0.005	-0.032	I		1.12	1.1
NGC 5129	-25.92	11.86	0.40	260	222	-0.115	0.116	0.024	0.029	I		4.27	4.8
NGC 5208	-25.61	11.73	0.61	270	235	-0.079		0.001	-0.024	B	13.0	5.01	15
NGC 5322	-25.51	11.68	0.05	246	239	-0.069		-0.002	-0.031	B	13.7	2.45	20
NGC 5490	-25.57	11.71	0.14	349	282	-0.227	0.104	0.056	0.020	I		2.14	9.5
NGC 5557	-25.46	11.66	0.04	279	223	-0.118	-0.118	0.015	-0.056	B	13.3	2.57	8.3
NGC 6223	-25.59	11.72	0.32	274	238	-0.192		0.008	0.006	B	13.5	1.55	6.0
NGC 6375	-25.53	11.69	0.24	226	187	-0.093		0.021	-0.042	I		1.17	1.5
UGC 10918	-25.75	11.79	0.03	247	249	-0.100	0.093	0.018	0.051	I		1.78	4.7
NGC 6482	-25.60	11.72	0.14	305	291	-0.102	-0.102	0.009	-0.033	B	13.1	1.58	1.0
NGC 6575	-25.58	11.72	0.12	264	234	-0.079		-0.011	-0.000	I		2.09	4.9
NGC 7052	-25.67	11.75	0.15	298	266	-0.102	-0.102	0.045	0.017	I		1.32	0.8
NGC 7242	-26.34	12.05	0.04	255	283	0.009	0.115	0.043	0.031	B	14.0	6.31	2700
NGC 7265	-25.93	11.87	0.04	230	206	-0.085	-0.085	-0.003	-0.061	B	14.7	6.92	5100
NGC 7274	-25.39	11.63	0.09	259	244	-0.091	0.137	0.030	0.003	S	14.7	6.92	3200
NGC 7386	-25.58	11.72	0.07	312	273	-0.064	-0.064	0.031	-0.003	B	13.9	2.57	3.1
NGC 7426	-25.74	11.79	0.56	284	219	-0.205	-0.205	0.031	-0.048	B	13.8	3.80	8.3
NGC 7436	-26.16	11.97	0.09	280	263	-0.124	0.208	0.043	0.022	B	14.4	4.07	100
NGC 7550	-25.43	11.65	0.04	270	224	-0.187	-0.187	0.005	-0.030	B	11.9	0.93	1.0
NGC 7556	-25.83	11.83	0.05	253	243	-0.012	0.082	0.029	0.049	B	14.0	2.00	17
NGC 7618	-25.44	11.65	0.25	292	265	-0.108	-0.108	0.022	-0.014	B	13.7	3.16	240
NGC 7619	-25.65	11.75	0.12	325	277	-0.128		0.020	-0.002	B	14.0	1.55	21
NGC 7626	-25.65	11.75	0.03	269	250	-0.201	-0.201	0.045	-0.019	S	14.0	1.55	21

Column notes: (1) Galaxy name, in order of increasing right ascension (not listed) for consistency with previous MASSIVE papers. (2)

Extinction-corrected 2MASS total absolute K -band magnitude. (3) Stellar mass estimated from M_K (eq. 2 of Ma et al. 2014, from Cappellari 2013). (4) Spin parameter λ within R_e . (5) Central fiber dispersion. (6) Average luminosity-weighted dispersion within R_e . (7) Power law slope of $\sigma(R)$ between 1 kpc to 2 kpc. (8) Power law slope of $\sigma(R)$ between $0.8R_{\text{max}}$ to R_{max} . Left blank when R_{max} is too small to allow measurement of γ_{outer} (see text). (9) Average luminosity-weighted h_4 within R_e , with typical formal errors ~ 0.01 . (10)

Gradient in h_4 , defined as $\Delta h_4 / \Delta \log_{10} R$. (11) Group membership according to the 2MRS HDC catalogue: "B" for BGGs, "S" for satellites, "I" for isolated galaxies with fewer than 3 group members. Membership in Virgo, Coma, Perseus, or Abell clusters is listed.

(12) Halo mass according to the HDC catalogue, or from updated literature sources (see text) for Virgo, Coma, and Perseus. (13)

Large-scale galaxy overdensity from the 2M++ catalogue. (14) Local density in units of the mean K -band luminosity density $\bar{\nu} \sim 2.8 \times 10^8 L_\odot \text{Mpc}^{-3}$. (**) Additional columns will be included in the electronic version of the table, available on request, including

$\sigma(R)$ fit parameters γ_1 , γ_2 , and σ_0 and uncertainties on γ_{inner} and γ_{outer} .

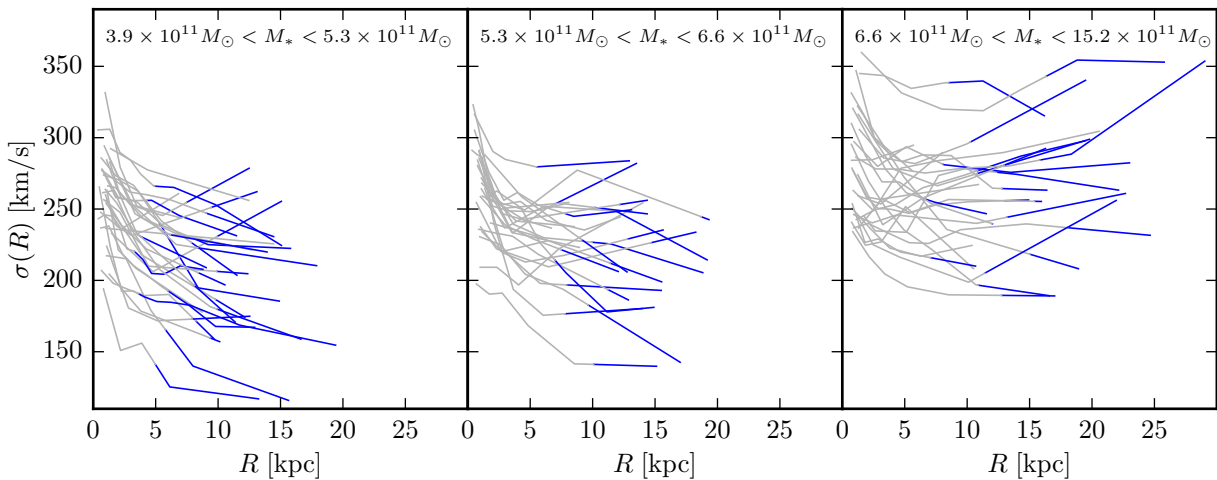


Figure 1. Stellar velocity dispersion profiles of 85 MASSIVE galaxies, calculated as a luminosity-weighted average of individual data points in each annulus. The 3 panels are arranged from low to high M_* , in equal-number bins corresponding to $-25.31 \text{ mag} > M_K > -25.60 \text{ mag}$ (left), $-25.60 \text{ mag} > M_K > -25.82 \text{ mag}$ (center), and $-25.82 \text{ mag} > M_K > -26.64 \text{ mag}$ (right). Each profile is blue at $R > R_e$. From left to right, the overall amplitude of σ increases, with more profiles rising and fewer steeply falling.

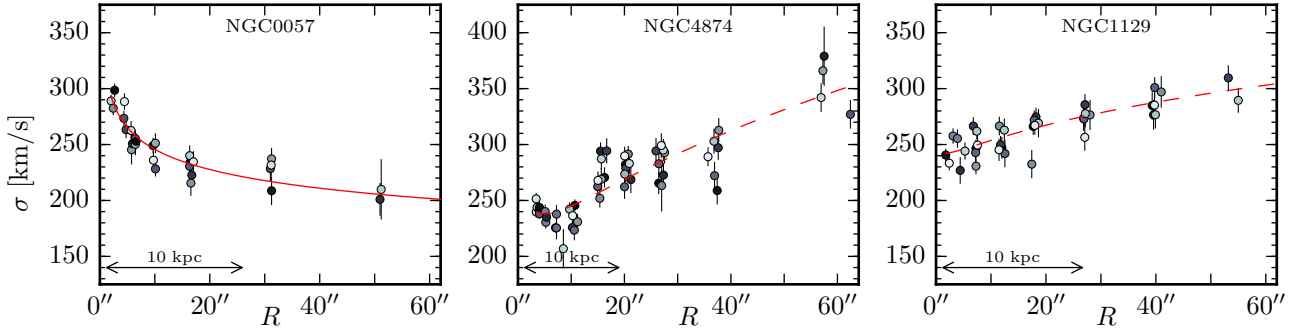


Figure 2. Examples of velocity dispersion profiles, with individual data points (black and white points near positive and negative major axis respectively, grey points near minor axis) and profile fits (red). Profile fits are either a single (solid) or double (dashed) power law. The majority of galaxies are fit by a declining single power law (left panel), but all galaxies with a substantial increase in σ at large radius require a broken power law whether they have an obvious minimum (middle panel) or rise monotonically (right panel).

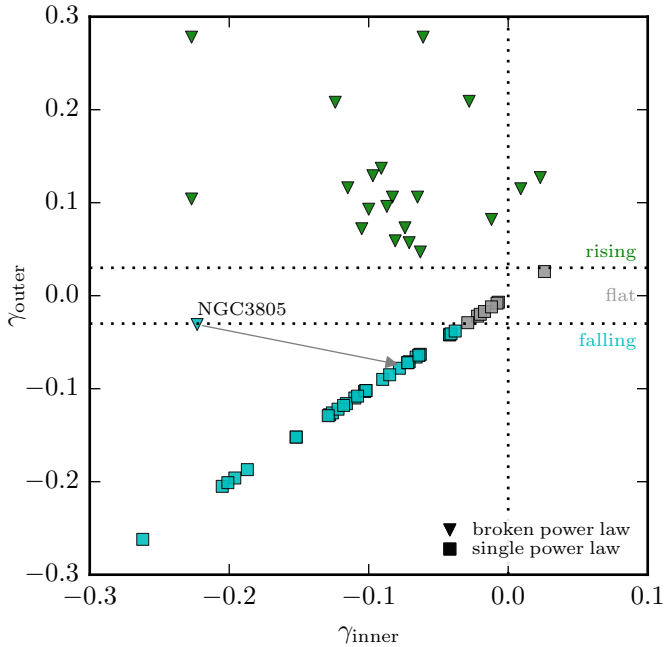


Figure 3. Outer vs. inner logarithmic slopes of $\sigma(R)$. Almost all γ_{inner} are negative, whereas γ_{outer} span ~ -0.3 to $\sim +0.3$. Galaxies fit by a single power law (squares) have $\gamma_{\text{inner}} = \gamma_{\text{outer}}$; all have slopes less than 0.03 (lower-left quadrant) and none has rising profiles. Galaxies fit by a broken power law (triangles) are mostly U-shaped (upper-left quadrant) with $\gamma_{\text{outer}} > 0.03$. NGC 3805 would move to (as indicated by the grey arrow) the diagonal line for single power-law galaxies if we computed the slopes using v_{rms} instead of σ ; it is a fast rotator and the only galaxy to change substantially from a broken to a single power law (see Section 3.2).

data cover sufficiently large field of view to measure γ_{outer} reliably (see Section 3.3 for details). Figure 3 shows γ_{inner} versus γ_{outer} for these 61 galaxies. In practice, this is qualitatively similar to the distribution of γ_1 vs γ_2 , except that the broken power law fits would be displaced towards the upper left by up to ~ 0.2 in extreme cases for γ_1 and γ_2 .

Of the 61 galaxies, we find 18 galaxies ($\sim 30\%$) to have a U-shaped profile with $\gamma_{\text{inner}} < 0$ and $\gamma_{\text{outer}} > 0$ (upper left quadrant); 2 galaxies ($\sim 3\%$) to have monotonically ris-

ing profiles ($\gamma_{\text{inner}} > 0$, $\gamma_{\text{outer}} > 0.03$, upper right quadrant); and 33 galaxies ($\sim 54\%$) to have monotonically falling profiles, all of which are well fit by a single power law with $\gamma_{\text{inner}} = \gamma_{\text{outer}} < 0.03$ (lower left quadrant). Eight of the 61 galaxies ($\sim 13\%$) have $|\gamma_{\text{outer}}| < 0.03$ (horizontal dashed lines in Figure 3), consistent with having a flat $\sigma(R)$ in the outer parts, and all 8 of these are well fit by a single power law (i.e. $\gamma_{\text{inner}} = \gamma_{\text{outer}}$).

We define rising, flat, and falling outer profiles to be those with $\gamma_{\text{outer}} \geq 0.03$, $-0.03 < \gamma_{\text{outer}} < 0.03$, and $\gamma_{\text{outer}} \leq -0.03$ respectively. Under this definition, all galaxies requiring a broken power law fit have rising outer profiles except for NGC 3805, which is one of our fastest rotators and is actually more similar to a typical monotonically falling profile (see Section 3.2).

Uncertainties on γ_{inner} and γ_{outer} depend both on the uncertainty on the observed σ , and on whether the dispersion profile contains bumps, wiggles, or other features not accounted for in this simple fit. Errors for single power law fits range from 0.005 to 0.04, while errors on both γ_{inner} and γ_{outer} for broken power law fits range from 0.02 to 0.08. NGC 3805 and UGC 10918 are exceptions, with errors on γ_{outer} of 0.15 and 0.17 respectively. NGC 3805 was discussed above. UGC 10918, with $\gamma_{\text{outer}} \sim 0.09$, is thus the most uncertain rising profile we have measured, but we do not single it out in any way in the remaining analysis. Errors for each galaxy are not tabulated in Table 1 but will be available in the electronic version of the table.

3.2 Effects of rotation: σ versus v_{rms}

Although many galaxies in the MASSIVE survey are slow or non-rotators (Veale et al. 2017a,b), 19 galaxies in the sample reported in this paper have spin parameter $\lambda_e \geq 0.2$ (see column 4 of Table 1), where the galaxy rotation V can contribute a non-negligible amount to the second velocity moment $v_{\text{rms}} \equiv \sqrt{V^2 + \sigma^2}$.

To quantify the effects of rotation, we re-calculate γ_{outer} using $v_{\text{rms}}(R)$ instead of $\sigma(R)$ and compare the two slopes in Figure 4. As expected, the effect of rotation is to make the v_{rms} profile decline less steeply than the σ profile. The changes in γ_{outer} due to the difference in v_{rms} and σ , however, are small (0.05 or less) and affect less than 20% of

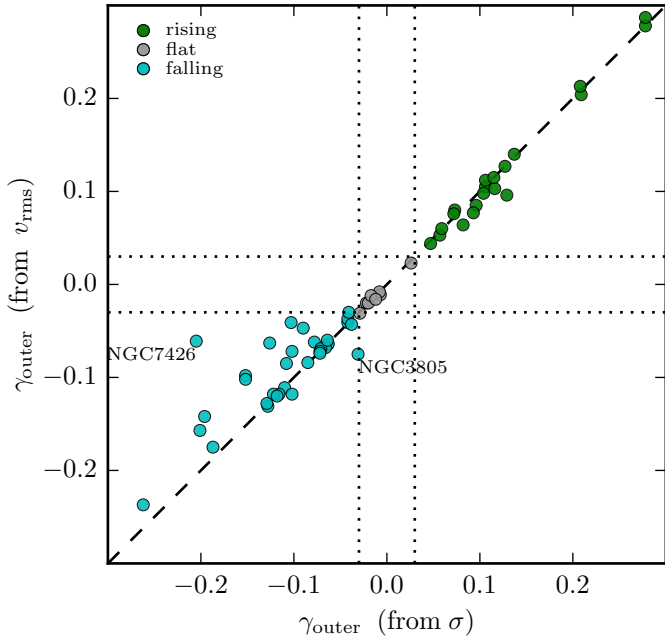


Figure 4. Comparison of γ_{outer} for $v_{\text{rms}}(R)$ and $\sigma(R)$. As expected, because v_{rms} is larger than σ for outer bins of fast rotators, the outer profile of $v_{\text{rms}}(R)$ is flatter than $\sigma(R)$ for a handful of galaxies. However, the difference in γ_{outer} is small overall since most galaxies in our sample are slow or non-rotators. Two examples of noticeable differences are labeled (see text): NGC 7426 is well fit by a single power law in both cases but with a much shallower slope for $v_{\text{rms}}(R)$ (-0.07 vs. -0.205); NGC 3805 changes from requiring a broken to a single power-law fit (see also Figure 3).

the sample. NGC 7426 shows the largest change in γ_{outer} (-0.205 from σ vs. -0.07 for v_{rms}), and is our second fastest rotator ($\lambda_e = 0.56$). NGC 3805 is our third fastest rotator ($\lambda_e = 0.50$), requiring a broken power law fit of $\gamma_{\text{inner}} = -0.22$ and $\gamma_{\text{outer}} = -0.031$ for $\sigma(R)$, but its $v_{\text{rms}}(R)$ is very well-fit by a single power law of slope -0.085 . We note that none of these changes alter the classification of NGC 7426 and NGC 3805 as having falling (outer) profiles. Other galaxies with noticeable changes in γ_{outer} tend to be fast rotators as well.

Because the differences in slopes and profile fits between $v_{\text{rms}}(R)$ and $\sigma(R)$ are generally small and do not impact our results presented below, we will use $\sigma(R)$ and the slopes computed from $\sigma(R)$ for the rest of the paper.

3.3 The importance of a large field of view

Our IFS data extend up to 40 kpc, with most galaxies in the 15–30 kpc range, corresponding to ~ 1 to $4R_e$. This is usually far enough to capture the transition from falling inner σ to rising outer σ in U-shaped galaxies, but a galaxy identified as U-shaped with data out to 30 kpc would likely appear to be monotonically decreasing if viewed to less than 10 kpc.

Figure 5 shows how the outer profile behaviour γ_{outer} relates to the outer boundary of our IFS data R_{max} . Indeed, none of the galaxies with $R_{\text{max}} < 18$ kpc are U-shaped, and all are well-fit by a single power law. Throughout the paper,

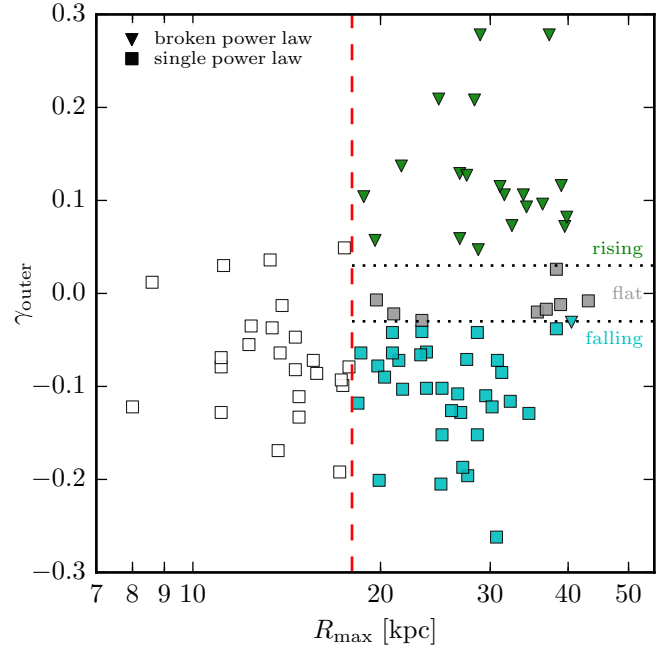


Figure 5. Outer $\sigma(R)$ slope γ_{outer} versus R_{max} , the maximum radius in kpc covered by our IFS data. None of the galaxies with $R_{\text{max}} < 18$ kpc show a clear transition from falling to rising σ , so we do not use γ_{outer} for those galaxies, since it is likely that our radial coverage is insufficient for a fair comparison to the rest of our sample. All of the galaxies with $R_{\text{max}} \geq 35$ kpc show (nearly) flat or rising profiles, but this is likely a coincidence (see text).

we will use γ_{outer} only from the 61 galaxies with $R_{\text{max}} > 18$ kpc. Galaxies with $R_{\text{max}} < 18$ kpc are considered to not have a good measurement of γ_{outer} , only a measurement of γ_{inner} .

There is some hint that γ_{outer} depends on R_{max} beyond 18 kpc, with none of the ~ 10 galaxies with the largest R_{max} having steeply falling γ_{outer} . However, we find no substantial difference in γ_{outer} when we re-fit the σ profile of those galaxies removing the outermost data (so long as the data still reach to 18 kpc). We conclude that there is no substantial bias in our sample between galaxies with $R_{\text{max}} \sim 20$ kpc and $R_{\text{max}} \sim 40$ kpc. Beyond $R_{\text{max}} \sim 40$ kpc, however, may be very different. We also cannot say conclusively that all galaxies with $R_{\text{max}} \sim 20$ kpc and steeply falling γ_{outer} would remain so if observed to $R_{\text{max}} \sim 40$ kpc. We do think it is unlikely that many of them would change substantially, since the galaxies with large R_{max} showed their flattened or rising behavior well before the outermost data points.

3.4 Comparison with literature

A number of the MASSIVE galaxies in this paper have published $\sigma(R)$ measurements, typically based on long-slit observations covering a smaller radial extent than our survey. In most cases, our results are reasonably consistent with these earlier measurements over comparable radial ranges, but our more extended data sometimes find different slopes for $\sigma(R)$ in the previously unexplored outer regions. In addition, our IFS data provide kinematic measurements over several an-

gular bins at a given radius. We discuss some specific cases here.

[Franx et al. \(1989\)](#) found falling $\sigma(R)$ profiles for NGC 1700, NGC 4472, and NGC 7619. We also find falling $\sigma(R)$ for all three galaxies, though with uniformly steeper power law slopes: -0.15 , -0.06 , -0.13 , instead of -0.03 , -0.02 , -0.08 , respectively, measured to uniformly larger radii (29, 14, 11 kpc, instead of 10, 2, 9 kpc respectively). Only NGC 1700 has a large enough radial extent for us to expect a reliable measurement of γ_{outer} , and it smoothly follows a single power law of slope -0.15 .

[Fisher et al. \(1995\)](#) found falling $\sigma(R)$ profiles for NGC 2832, NGC 4073, NGC 4472, NGC 4874, NGC 4889, and NGC 7619, with NGC 4839 nearly flat. Our inner slope γ_{inner} matches reasonably well with their power law slopes in all cases, where our (their) values are -0.07 (-0.07), -0.07 (-0.04), -0.06 (-0.04), -0.06 (-0.09), -0.11 (-0.05), -0.13 (-0.10), and 0.04 (-0.01), respectively. We find a positive outer slope γ_{outer} for all four galaxies for which we have measurements beyond 20 kpc: NGC 2832, NGC 4073, NGC 4874, and NGC 4889. None of their measurements covered beyond 20 kpc except for NGC 2832, which went to ~ 23 kpc. Our data for NGC 2832 extend to 33 kpc and find σ to increase in this outer region.

Another series of papers presented long-slit data of some MASSIVE galaxies (typically to a radius of $\sim 20''$), but did not quote power-law slopes of the σ profiles ([Simien & Prugniel 1997, 1998, 2000](#)): NGC 0080, NGC 0410, NGC 0890, NGC 1573, NGC 1684, NGC 2340, NGC 3158, and NGC 5129 were included. Many have large error bars on the σ profiles, but when trends can be discerned, all galaxies have flat or falling $\sigma(R)$ and agree with our measurements where they overlap. The two possible exceptions are NGC 1684 and NGC 3158. We see a large scatter in σ in the outskirts of NGC 1684, but no coherent increase, so the few outer points from [Simien & Prugniel \(2000\)](#) are likely part of that scatter rather than indicating a true increase. For NGC 3158, we do see a small bump in σ at the outskirts of the [Simien & Prugniel \(1998\)](#) measurement, but we find that σ remains flat beyond that radius. Of these 8 galaxies, we find two galaxies (NGC 0080 and NGC 5129) to show rising σ beyond $20''$.

A few individual galaxies have also been studied previously: NGC 1600 ([Verolme et al. 2002](#)), NGC 2320 ([Cretton et al. 2000](#)), and NGC 2672 ([Bonfanti et al. 1995](#)), and they similarly agree with our measurements where they overlap. None of those galaxies show rising σ in our sample. On the other hand, of the five galaxies with data in both this paper and [Loubser et al. \(2008\)](#) (NGC 2832, NGC 3842, NGC 4839, NGC 4874, and NGC 4889), only NGC 3842 shows a falling outer profile in our data. NGC 4839 shows a roughly flat $\sigma(R)$ over our limited radial extent, and the remaining three all have rising outer $\sigma(R)$. In all three cases, our data extend farther than that in [Loubser et al. \(2008\)](#) and agree with their data in the inner regions.

Many galaxies in the Coma cluster have falling $\sigma(R)$ ([Thomas et al. 2007](#)), but that paper found all three Coma galaxies in the MASSIVE sample (NGC 4839, NGC 4874, and NGC 4889) to have at least some hint of a rising profile. Of those, NGC 4839 had the most prominent rise, and was also the only galaxy to be measured to (and slightly beyond) R_e . In our sample, the situation is reversed, with NGC 4839

measured to less than 10 kpc and showing only a slight rise while NGC 4874 and NGC 4889 are measured to at least 30 kpc and show a substantial rise in σ .

We have also compared those of our galaxies that overlap with ATLAS^{3D} (NGC 4472, NGC 5322, and NGC 5557) in Appendix B of [Veale et al. 2017a](#) and find that all the kinematics (not just σ) match well where they overlap in radius. None of these three galaxies are in the subset of ATLAS^{3D} galaxies studied in the SLUGGS survey ([Foster et al. 2016](#)).

4 DISPERSION PROFILES VERSUS VELOCITY KURTOSIS h_4

When interpreting dispersion profiles, the degeneracy between velocity anisotropy and enclosed mass (or mass-to-light ratio) can be somewhat alleviated by examining the kurtosis h_4 of the LOSVD. Radial anisotropy is generally associated with positive h_4 and lower projected σ , while tangential anisotropy is associated with negative h_4 and higher projected σ ([Gerhard et al. 1998](#)). Even in isotropic systems, however, positive h_4 can also arise from gradients (of either sign) in circular velocity ([Gerhard 1993](#); [Baes et al. 2005](#)). A transition from the galaxy dispersion to cluster dispersion can also be interpreted as a galaxy surrounded by intracluster light (ICL) from a diffuse halo of stars controlled by the cluster gravity, although a clear decomposition into these two components is difficult ([Bender et al. 2015](#)). In practice, for cluster BCGs (especially cD galaxies) an ICL component and a circular velocity gradient play similar roles for our purposes, both producing a positive h_4 .

[Figure 6](#) shows that, as we found in [Veale et al. \(2017a\)](#), MASSIVE galaxies have generally positive h_4 and there is evidence for a correlation between outer σ gradient and h_4 gradient. The p -value for the significance of the correlation (with correlation coefficient 0.42) is 7×10^{-5} . One feature not found in [Veale et al. \(2017a\)](#) are the few galaxies with negative $\langle h_4 \rangle$ and substantially negative (< -0.1) gradients in h_4 . These are likely due to low σ , with $\sigma < 200$ km/s causing large scatter in h_4 because of limitations on wavelength resolution. In particular, the most negative two points in both panels of [Figure 6](#) and the outlying positive h_4 gradient are all galaxies with low average σ . Because [Veale et al. \(2017a\)](#) focused only on the most massive 41 galaxies of the sample, it is not surprising that outliers related to low σ did not arise in that subsample. Formal errors on $\langle h_4 \rangle$ are typically ~ 0.01 , but additional systematic effects are likely present for low σ .

As in [Veale et al. \(2017a\)](#), we argue the correlation between the h_4 gradient and γ_{outer} is much more likely to be a consequence of circular velocity gradients (or an ICL component) than velocity anisotropy. If all galaxies had similar mass (and light) profiles, then a positive h_4 gradient related to greater radial anisotropy at large radius would be expected to accompany a more *negative* σ gradient, and so cannot explain the observed correlation. It is also true that tangential anisotropy can only boost σ by a limited amount, and in particular cannot boost it above the circular velocity. This makes invoking radial anisotropy to explain low σ more easily justified in most cases than invoking tangential anisotropy to explain high σ . For these reasons, we argue

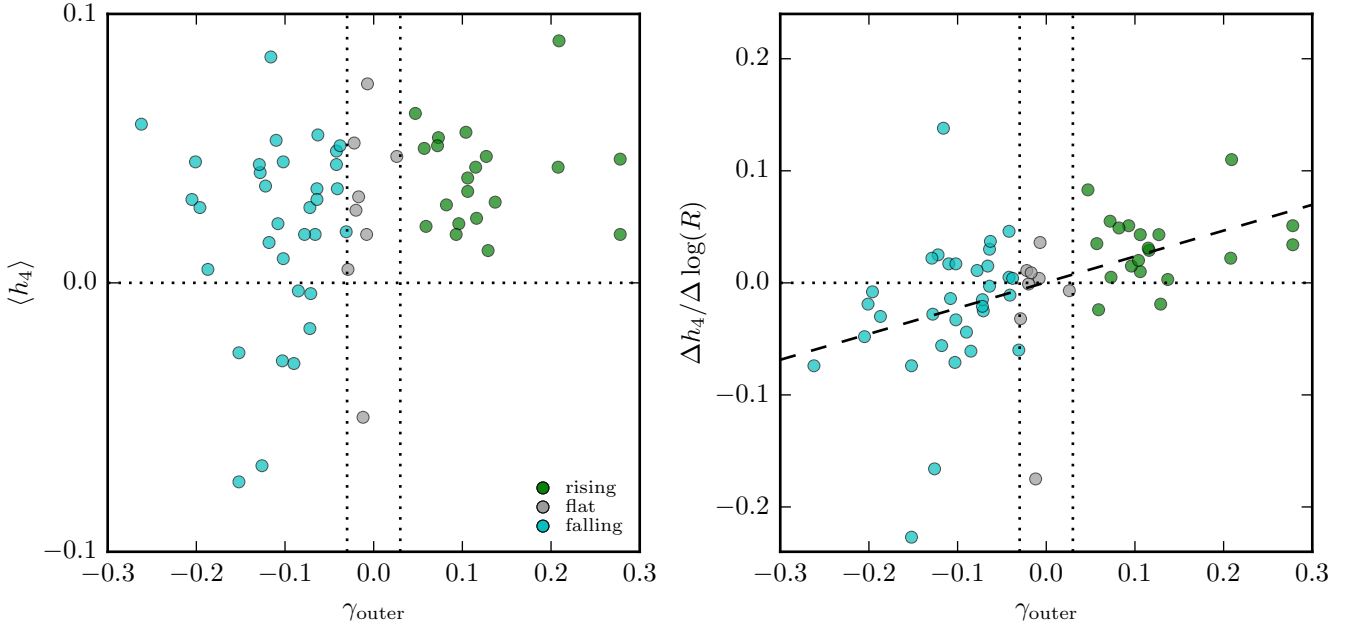


Figure 6. Luminosity-weighted average h_4 within R_e (left) and h_4 gradient (right) versus γ_{outer} . All galaxies with rising outer $\sigma(R)$ profiles have positive $\langle h_4 \rangle$. There is a positive correlation between h_4 gradient and γ_{outer} (dashed line in right panel) with a correlation coefficient of 0.42, and the corresponding p -value for the significance of the correlation is $p = 7 \times 10^{-5}$. The few outliers in both panels are galaxies with low overall σ perhaps due to limitations on spectral resolution.

that variations in the total mass profiles across our sample (and variations from isothermal profiles) are likely present.

In this context, our positive $\langle h_4 \rangle$ could result from either mass profiles (V_{circ} gradients/ICL components) or radial anisotropy, or some combination of both. If mass profiles are the dominant effect on h_4 , then in principle *tangential* anisotropy may also be common in our sample in spite of the overall positive h_4 . Based on our data, we can make no claims about the anisotropy of our sample as a whole, or about changes in anisotropy across our sample, without more detailed dynamical modeling. We leave such modeling for future papers.

5 DISPERSION PROFILES VERSUS GALAXY MASS AND ENVIRONMENT

5.1 σ profiles and stellar mass M_*

Figure 7 shows the inner slope γ_{inner} (left) and outer slope γ_{outer} (right) of $\sigma(R)$ versus stellar mass M_* (and M_K) for the 85 MASSIVE galaxies (61 of which have reliable γ_{outer} ; see Section 3.3). Most galaxies have falling $\sigma(R)$ in the inner part ($\gamma_{\text{inner}} \lesssim 0$), but the outer $\sigma(R)$ has slopes spanning $-0.3 \lesssim \gamma_{\text{outer}} \lesssim 0.3$. Thick black pentagons indicate the average values of γ_{inner} and γ_{outer} for each of the three M_* bins. Both γ_{inner} and γ_{outer} show a positive trend with M_* . In particular, the 11 most massive galaxies ($M_* \gtrsim 8 \times 10^{11} M_\odot$) all have flat or rising outer $\sigma(R)$, with a positive average slope $\langle \gamma_{\text{outer}} \rangle \approx 0.1$ (right panel). Most of them also do not have steeply falling inner $\sigma(R)$, where the individual γ_{inner} are above ~ -0.1 , and the average γ_{inner} is only slightly below 0. For the lower two stellar mass bins, the distribution of γ_{inner}

is similar whether the outer profile is rising (green) or falling (blue), with averages of those subsamples well within errors of each other.

Figure 8 shows the fraction of galaxies with rising (green), flat (grey), and falling (cyan) outer $\sigma(R)$ for the three M_* bins. This figure again shows the prevalence of galaxies with rising outer σ at high M_* . The error bars² in Figure 8 reflect the uncertainty due to small number statistics in each bin. Another source of uncertainty is the possibility of a galaxy size bias relating to R_{max} : our most massive galaxies tend to have larger R_{max} in kpc, which could in principle impact the measurement of γ_{outer} . However, as discussed in Section 3.3, re-calculating γ_{outer} for galaxies with large R_{max} without the outermost data gives very similar results, so the trend in Figure 8 is not simply due to a bias in R_{max} .

As discussed in Section 4, detailed mass modeling would be needed to determine whether the correlations between γ_{outer} and M_* seen in Figure 7 and Figure 8 indicate mass profile changes, or velocity anisotropy variations, or both. Dynamical and lensing measurements have found roughly isothermal total mass profiles for many elliptical galaxies, especially within one or two R_e (Gerhard et al. 2001; Treu et al. 2006; Koopmans et al. 2009; Auger et al. 2009, 2010; Thomas et al. 2011; Sonnenfeld et al. 2013; Cappellari et al. 2015). But there is some evidence that smaller galaxies may have steeper than isothermal mass profiles (Romanowsky et al.

² Error bars are calculated as described in Appendix B of Veale et al. (2017b), with a Beta distribution as prior and posterior. We use $n_{\text{prior}} = 2$ for a very weak prior, and μ_{prior} is the total sample fraction of rising (20/61) or falling (33/61) profiles.

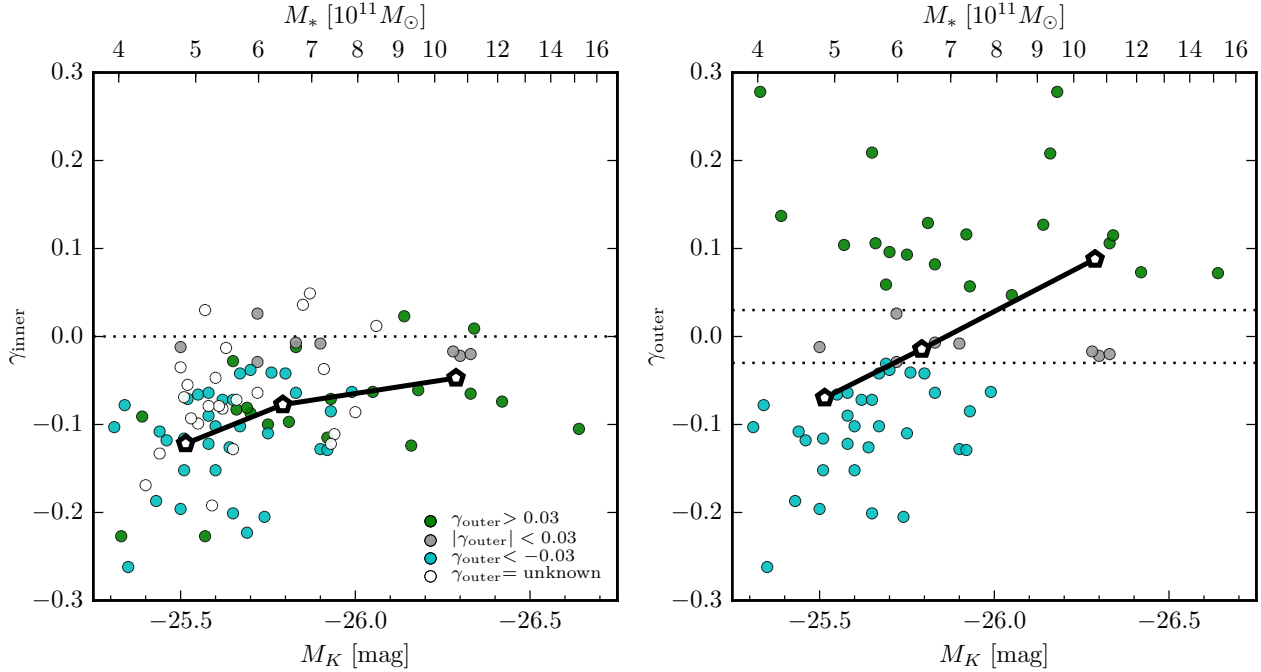


Figure 7. Inner (left) and outer (right) slopes of $\sigma(R)$ versus M_* (and M_K). The inner σ profiles are mostly falling, but the average power-law slope (thick black pentagons) becomes less negative with each increasing M_* bin. The outer slopes γ_{outer} span -0.3 to $+0.3$ at the lower mass but are mostly positive at $M_* \gtrsim 8 \times 10^{11} M_\odot$. Rising outer profiles are found across the whole mass range, whereas falling outer profiles are found only for galaxies with $M_* \lesssim 8 \times 10^{11} M_\odot$.

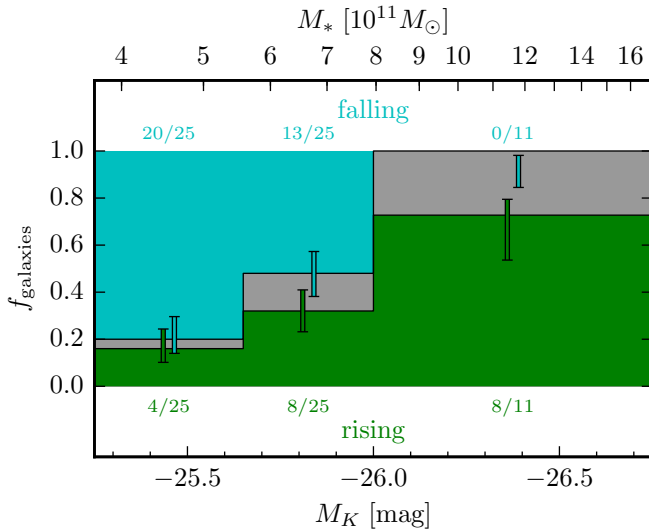


Figure 8. Fraction of rising (green), flat (grey), and falling (cyan) outer σ profiles versus M_K and M_* . We classify galaxies with $\gamma_{\text{outer}} \geq 0.03$ as rising, those with $\gamma_{\text{outer}} \leq -0.03$ as falling, and those in between as flat.

2003; Napolitano et al. 2009; Deason et al. 2012; Morganti et al. 2013; Alabi et al. 2016), whereas more massive galaxies may have shallower than isothermal profiles (Newman et al. 2013). Simulations have suggested that merger histories may influence velocity anisotropy (Dekel et al. 2005; Wu et al. 2014), so the fact that more massive galaxies have

a more extensive merger history may also link mass to velocity anisotropy.

In all of these cases, it is important to keep in mind the physical scale under consideration: at small radii, central supermassive black holes become important, while stars dominate at intermediate radii and dark matter dominates at large radii. For example, core scouring by merging supermassive black holes likely impacts the σ profiles near the galaxy center (Thomas et al. 2014) and may relate to γ_{inner} . The IFS data presented here do not resolve the galaxy cores, however, so we will not consider further the central regions of the galaxy and γ_{inner} . In the following sections we focus instead on how the outer σ profiles (i.e. γ_{outer}) may correlate with galaxy environment and dark matter.

5.2 Outer σ profiles vs. environmental measures M_{halo} , δ_g , and ν_{10}

Figure 9 shows the outer σ slope γ_{outer} (upper panels) and the fraction of galaxies with rising, flat, and falling outer σ profiles (lower panels) versus three environmental variables: halo mass M_{halo} (left), large-scale overdensity δ_g (middle), and local density ν_{10} (right). Within each upper panel, the average γ_{outer} for three environmental bins is shown as thick black pentagons. All panels show clear trends of increasing f_{rising} , increasing average γ_{outer} , and decreasing f_{falling} in denser environments, and the trend is most prominent for M_{halo} .

The upper panels of Figure 9 also show that galaxies with rising outer $\sigma(R)$ are found preferentially in high density environments, while galaxies with declining outer

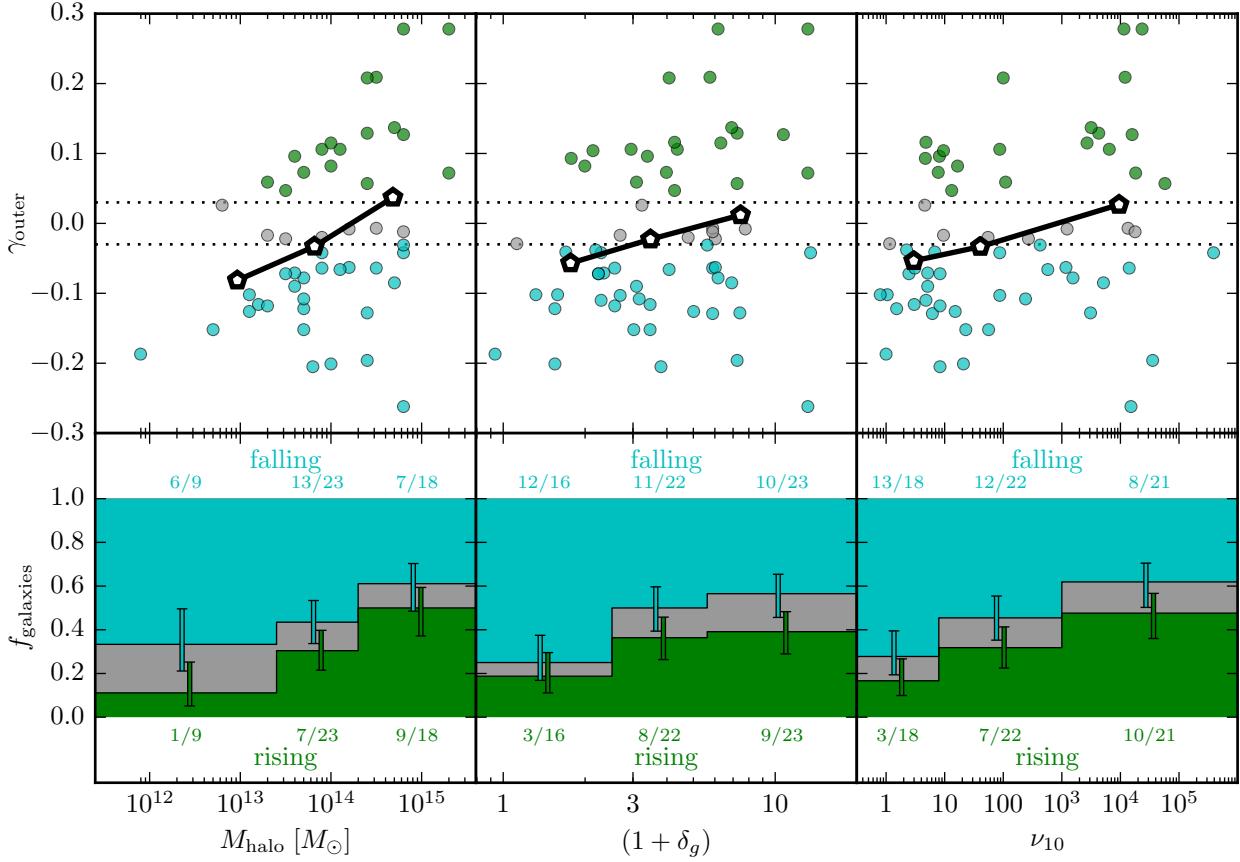


Figure 9. Outer $\sigma(R)$ profile behavior versus three environment measures: M_{halo} (left), large-scale density δ_g (middle), and local density ν_{10} (right). The top panels show γ_{outer} ; the bottom panels show the fraction of rising (green), flat (grey), and falling (cyan) outer profiles. For all three environmental measures, f_{rising} and average γ_{outer} (open black pentagons) increase in more dense environments, and f_{falling} decreases correspondingly. The environmental dependence is strongest with M_{halo} . The most steeply rising outer profiles are also found in the highest density environments, while falling profiles are found in the full range of environments.

Table 2. Two-sample Kolmogorov-Smirnov test D statistic and p values for comparing the distribution in M_* or environment of the galaxy sample, split into two samples of galaxies by separating first rising profiles (left columns) and then falling profiles (right columns).

	(rising v. flat+falling)		(rising+flat v. falling)	
	D -statistic	p -value	D -statistic	p -value
M_K	0.356	0.050	0.456	0.002
M_{halo}	0.337	0.073	0.285	0.142
δ_g	0.285	0.186	0.315	0.078
ν_{10}	0.305	0.133	0.271	0.183

$\sigma(R)$ span the full range of environments. In terms of halo mass, the galaxies with $\gamma_{\text{outer}} > 0.03$ have an average M_{halo} of $4.4 \times 10^{14} M_{\odot}$, about three times more massive than the average M_{halo} of $1.6 \times 10^{14} M_{\odot}$ for galaxies with $\gamma_{\text{outer}} < -0.03$.

We have performed a two-sample Kolmogorov-Smirnov (KS) test to compare the distributions of galaxy mass and environments, first comparing galaxies with rising profiles to those with flat or falling profiles, and second comparing galaxies with falling profiles to those with flat or rising ones. Table 2 shows both the D statistic, which measures

the maximum difference between the empirical cumulative distribution functions of the two samples, and the p -value, which quantifies the significance of that difference taking into account sample size.³

We find that the most significant difference between the samples is related to the decrease in f_{falling} with increasing M_* , as expected from Figure 8, with $p \sim 0.002$. The next two most significant differences are related to the increase in f_{rising} with increasing M_* ($p \sim 0.05$) and M_{halo} ($p \sim 0.07$). There is an interesting feature of separating strongly rising and falling profiles from flat ones: while both M_* and M_{halo} have comparable p -values when separating rising profiles, the p -value for separating falling profiles becomes much smaller for M_* but much larger for M_{halo} . This indicates that different mechanisms may be behind the two trends, and we will discuss this further in Section 6.

Much like the situation with M_* in Section 5.1, the cor-

³ We have adjusted the p -value of the KS test for distributions in M_{halo} to account for the reduced sample size, due to some galaxies being isolated with no measurement of M_{halo} available, by using the full sample size including isolated galaxies when converting the D -statistic to a p -value. This reduces the p -values from $\sim 0.13, 0.24$ to $\sim 0.07, 0.14$.

relation between σ profile behaviour and environment may be related to changing mass and luminosity profiles, changing velocity anisotropy, or both. Based on our results in Section 4, we find it unlikely that anisotropy alone can be behind the correlation. Instead, we interpret this as evidence that galaxies in more massive haloes may have total mass profiles that are shallower than isothermal, while those in less massive haloes have the more “typical” isothermal profiles. Some lensing results have also suggested this (Newman et al. 2015). We cannot entirely rule out anisotropy playing some role, however. The connection between merging history and anisotropy may also result in a connection between environment and anisotropy, since galaxies in more dense environments likely experience a more extensive merger history. This parallels our discussion from Section 5.1, and indeed the correlation between M_* and environment makes the two arguments equivalent to some degree. We will explore in the next sections how to distinguish whether trends with M_{halo} are simply a reflection of trends in M_* , or vice versa, or whether both are independent.

5.3 Outer σ profiles vs. group membership

Figure 10 and Figure 11 show $\sigma(R)$ for the 85 MASSIVE galaxies sorted by group membership, i.e., whether it is the brightest galaxy or a satellite in a group/cluster, or it is relatively isolated. The differences in the fractions of rising or falling profiles for the three types are small in comparison to the differences with M_* or M_{halo} .

The right side of Figure 11 shows the γ_{outer} versus M_* and M_{halo} panels of Figure 7 and Figure 9, but with group membership marked with additional symbols (magenta squares are isolated; orange diamonds are satellites; unmarked galaxies are all BGGs). The satellite galaxies in our sample, as expected, are found only in the higher mass haloes ($M_{\text{halo}} \gtrsim 10^{14} M_{\odot}$); in the lower mass haloes, only the BGGs are luminous enough to pass our survey magnitude cutoff. Satellite galaxies also reside in the lower part of the M_* range. The average γ_{outer} for satellite galaxies is very similar to that for BGGs or isolated galaxies, with the effects of increased γ_{outer} with both M_* and M_{halo} largely cancelling each other. The standard deviation on γ_{outer} for satellites, however, is markedly larger: 0.17 for satellites, compared to 0.09 for isolated galaxies and 0.10 for BGGs.

The physical significance of rising σ in BGG and satellite galaxies may be different, especially if rising σ is connected to the total mass profiles. In many discussions (e.g. Bender et al. 2015) the focus is on a central galaxy in a large cluster, and the total mass profile is simply the combination of stellar mass and the dark matter of the cluster halo. Ongoing detailed mass modeling of our satellite galaxies will help elucidate the impact of the group or cluster halo mass on a non-central galaxy, which may have its own dark matter subhalo or be moving at a substantial velocity relative to the group or cluster rest frame.

Figure 11 shows that 3 of the 11 isolated galaxies with reliable γ_{outer} in our sample have rising profiles (NGC 5129, NGC 5490, and UGC 10918). All three have relatively large uncertainties on γ_{outer} (> 0.05), especially UGC 10918 (see Section 3.1). All three galaxies are at fairly large distances (108, 79, and 100 Mpc, respectively). If we assume they are BGGs of groups whose rank 3 members fall just below the

2MASS limit, they will have luminosity gaps (~ 2.0 mag) comparable to those found for some other BGGs in our sample. Only about 10 of our 85 galaxies have luminosity gaps (between rank 1 and rank 3) as large as 2.0 mag, and all 10 of those galaxies have $M_{\text{halo}} < 10^{14} M_{\odot}$. These three isolated galaxies would thus be unusually fossil-like if they reside in halos of $M_{\text{halo}} \gtrsim 10^{14} M_{\odot}$. If they instead reside in smaller halos, their group composition may be comparable to that of many BGGs in our sample, but they would then have γ_{outer} as high or higher than all our other BGGs at those halo masses.

5.4 Untangling the joint relationships of M_* and M_{halo}

In this section we consider two opposing, extreme assumptions: first, that the probability of a galaxy having a rising σ profile (denoted P_{rising}) is a function of M_* (or M_K) only, and second, that it is a function of M_{halo} only. If $P_{\text{rising}} = P_{\text{rising}}(M_*)$, and M_{halo} plays no direct/independent role in influencing the σ profile, we still expect some residual correlation between the measured fraction of rising profiles (f_{rising}) and M_{halo} . This arises because the distribution of M_* changes with M_{halo} for our sample, so convolving $P_{\text{rising}}(M_*)$ with that distribution gives a fraction of rising profiles that depends on M_{halo} . The reverse also applies: if $P_{\text{rising}} = P_{\text{rising}}(M_{\text{halo}})$ then the connection between M_{halo} and M_* results in some correlation between f_{rising} and M_* .

Figure 12 compares the “predictions” of each of these extreme assumptions with the actual measured f_{rising} . The test samples used to calculate f_{rising} for the two assumptions (i.e. using $P_{\text{rising}}(M_*)$ and $P_{\text{rising}}(M_{\text{halo}})$) are constructed by assigning each galaxy in our sample a *probability* of having a rising profile, then running 1000 Monte Carlo trials assigning falling/rising profiles according to those probabilities and counting the resulting fractions in each bin. $P_{\text{rising}}(M_*)$ is constructed by fitting a logistic function to the unbinned M_* data (where falling profiles are 0 and rising profiles are 1), and similarly for M_{halo} .⁴

In each case, the test sample accounts for some, but not all, of the increase in f_{rising} with M_* or M_{halo} , indicating that both M_* and M_{halo} are responsible for the trends in f_{rising} . This is in contrast to the case of fast and slow rotators in Veale et al. (2017b), where M_* alone determines P_{slow} (within errors). It also differs from the case of f_{falling} in this paper; unsurprisingly, since the change in f_{falling} is much steeper for M_K than M_{halo} , we find that using $P_{\text{falling}}(M_*)$ to construct $f_{\text{falling}}(M_{\text{halo}})$ is consistent with the observed fraction, while using $P_{\text{falling}}(M_{\text{halo}})$ to construct $f_{\text{falling}}(M_*)$ does not account for the observed fraction.

We can also ask whether $P_{\text{rising}}(M_*)$ or $P_{\text{rising}}(M_{\text{halo}})$ does better at “predicting” the fraction of galaxies with rising profiles as a function of the other environment measures. Figure 13 shows that both $P_{\text{rising}}(M_*)$ and $P_{\text{rising}}(M_{\text{halo}})$ generate f_{rising} versus δ_g , v_{10} , and group membership that matches reasonably well to the data. However, the $P_{\text{rising}}(M_{\text{halo}})$ result

⁴ The 15 galaxies with no M_{halo} measurement are treated separately, each having a 3/15 (20%) probability of having a rising profile.

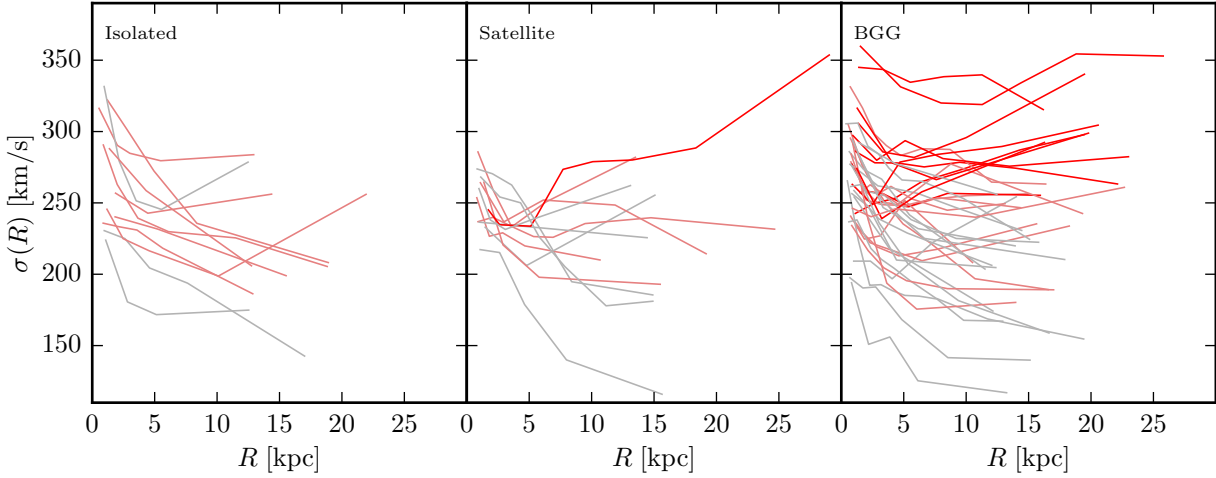


Figure 10. Dispersion profiles as in Figure 1, but separated by group membership status. The line colors correspond to the 3 bins of M_* in Figure 8, with grey for the least massive and red for the most massive. Ten of the most massive 11 galaxies in our sample are BGGs; the exception is NGC 4874, the second brightest galaxy in the Coma cluster.

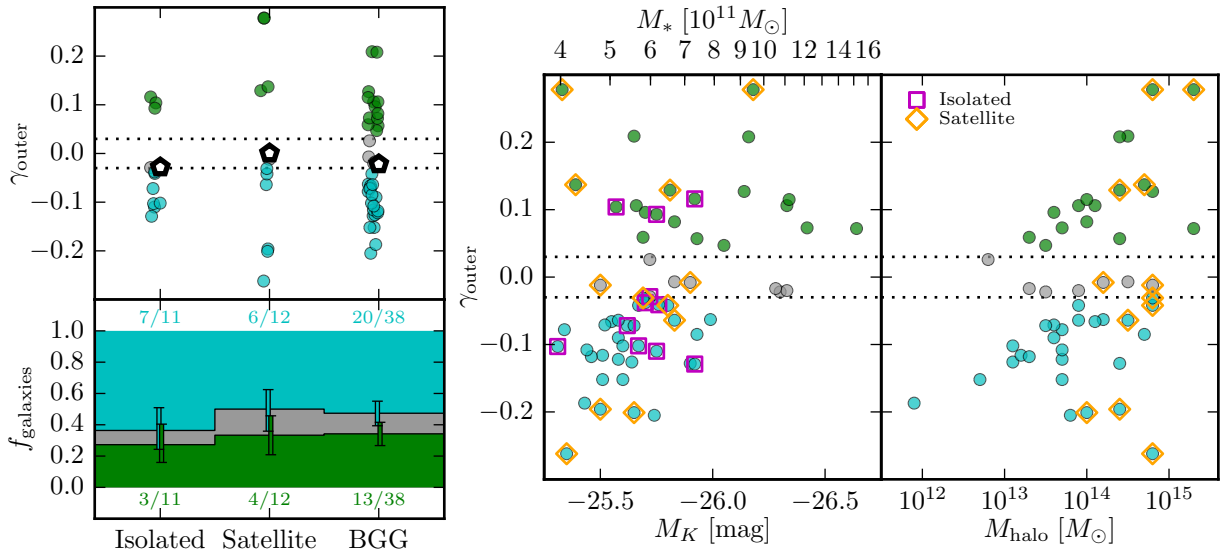


Figure 11. Outer slope γ_{outer} and fraction of rising (green), flat (grey), and falling (cyan) galaxies versus group membership status (left panels), and γ_{outer} versus stellar and halo masses with group membership highlighted (right panels). The average γ_{outer} (open black pentagons) is similar for all three membership types: -0.03 , 0.0 , and -0.02 for isolated, satellite, and BGG respectively. Satellite galaxies (yellow diamonds) include the most steeply rising and falling σ profiles. This may be related to the fact that satellite galaxies occupy the lower part of the M_* range and the upper part of the M_{halo} range; γ_{outer} tends to increase with both M_* and M_{halo} , so the two correlations cancel each other to give similar average γ_{outer} for satellite galaxies, but give satellite galaxies the largest spread in γ_{outer} .

matches slightly more closely to $f_{\text{rising}}(v_{10})$, which is not surprising because M_{halo} and v_{10} are quite closely correlated. On the other hand, the $P_{\text{rising}}(M_*)$ result matches slightly more closely to $f_{\text{rising}}(\delta_v)$. Interestingly, the group membership status shows the largest difference between “predictions” using M_* and M_{halo} , in the satellite galaxies, and the actual fraction falls precisely in the middle. Given the small number statistics of our satellite galaxies, the true fraction could easily fit either case.

6 CONCLUSIONS

We have measured and characterized the line-of-sight stellar velocity dispersion profiles $\sigma(R)$ of 85 early-type galaxies in the MASSIVE survey, spanning K -band magnitude $-25.3 > M_K > -26.7$, or stellar mass $4 \times 10^{11} M_{\odot} < M_* < 2 \times 10^{12} M_{\odot}$. Our IFS data cover $107'' \times 107''$ field of view and extend up to 40 kpc in radii, with most galaxies in the 15-30 kpc range. We find a radial coverage to ~ 20 kpc or beyond is necessary to measure the outer dispersion profiles of local massive ETGs (Figure 5).

We find three general shapes for $\sigma(R)$: monotonically

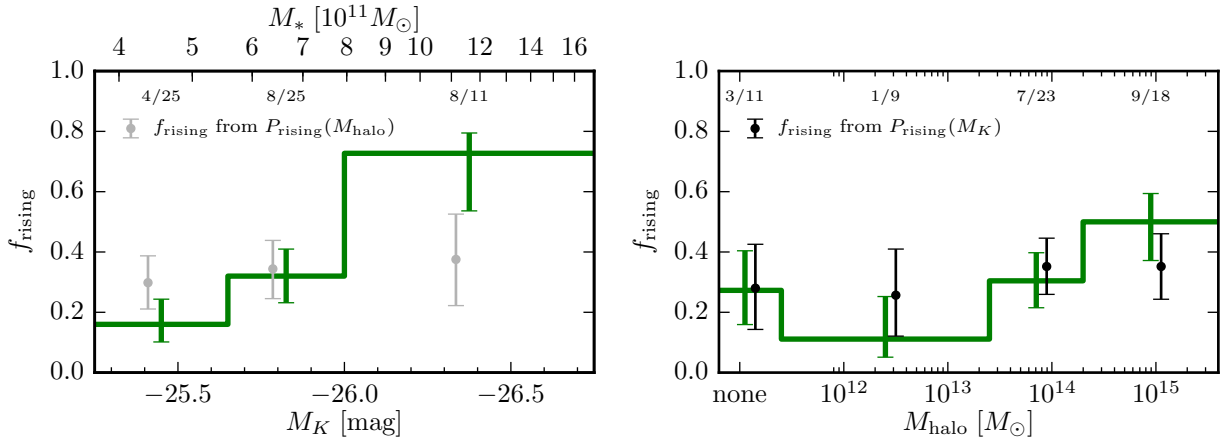


Figure 12. Comparing the assumptions that the probability of having a rising $\sigma(R)$ profile (P_{rising}) is a function of M_{halo} only (gray; left panel), or a function of M_K only (black; right panel). In each case P_{rising} is a logistic function fit to the data, with each galaxy at 0 (falling) or 1 (rising), so it is independent of the choice of binning. P_{rising} is used to calculate f_{rising} via 1000 Monte Carlo trials (see text). This is compared to the actual measured f_{rising} (green lines), with points offset slightly in the x-direction for clarity. The assumption that P_{rising} is a function only of M_{halo} does not predict the observed sharp increase in f_{rising} with M_K (left panel). Likewise, the assumption that P_{rising} is a function only of M_K produces a slight increase in f_{rising} versus M_{halo} , but not enough to match the data (right panel). Both stellar and halo masses therefore drive the observed trend in f_{rising} .

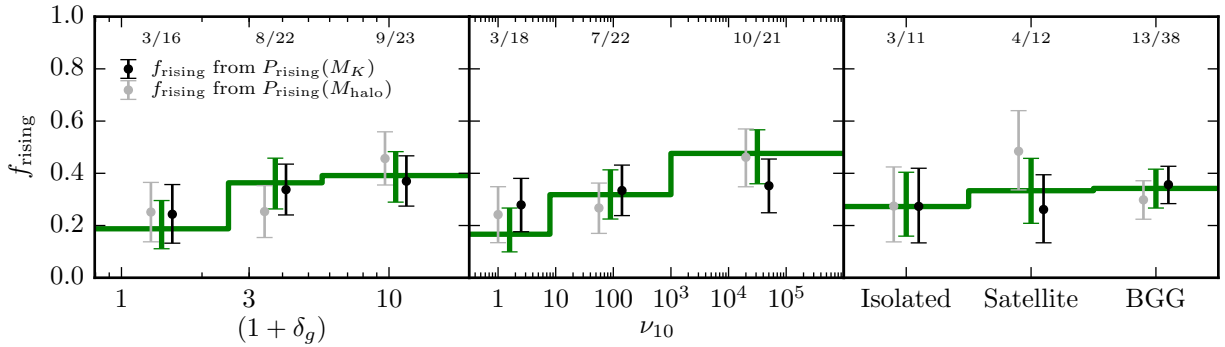


Figure 13. Comparing how well f_{rising} versus δ_g , ν_{10} and group membership status is reproduced under the assumption that P_{rising} is a function of M_K only (black) or of M_{halo} only (gray). One or both of these assumptions can reproduce the actual measured f_{rising} (green lines) in every case. Points within each bin are offset slightly for clarity.

falling, "U" shaped, or monotonically increasing (Figure 2). We quantify the shapes of $\sigma(R)$ with an inner and an outer logarithmic slope (γ_{inner} and γ_{outer}). All but 6 galaxies in our sample have negative γ_{inner} (Figure 3 and Table 1), with the 6 positive γ_{inner} all being close to 0 ($\gamma_{\text{inner}} < 0.05$). By contrast, γ_{outer} ranges from ~ -0.3 to $+0.3$, where 33% have rising outer $\sigma(R)$ ($\gamma_{\text{outer}} \geq 0.03$), 13% have flat profiles ($|\gamma_{\text{outer}}| < 0.03$), and 54% have falling profiles ($\gamma_{\text{outer}} \leq -0.03$; Figure 3).

We show that the fraction of galaxies with rising outer $\sigma(R)$ profiles increases significantly over our M_* range (Figure 7, Figure 8). That fraction also increases in denser environments, as quantified by halo mass M_{halo} , large-scale density δ_g , and local density ν_{10} (Figure 9). Among those, the trend is most prominent with M_{halo} , with the steepest rising profiles belonging to galaxies in the highest mass haloes.

We find that the probability of a galaxy having a rising outer σ profile cannot be adequately expressed as either a function of M_* alone or as a function of M_{halo} alone (Figure 12). Both M_* and M_{halo} are therefore responsible for driving the trends in the rising fraction. This is to be

contrasted with galaxy rotation in the previous MASSIVE paper (Veale et al. 2017b), where the sharp increase in the fraction of slow rotators with M_* is enough to explain the correlation between galaxy rotation and all environmental measures including M_{halo} . The first and second velocity moments of massive galaxies therefore reflect different aspects of their past assembly histories.

We do not detect significant difference in the distributions of γ_{outer} when the galaxies are grouped as BGGs, satellites, or isolate (Figure 11). Rising dispersion profiles are not limited to BGGs but are found for all three types of galaxies with comparable rates ($\sim 30\%$). Compared to the BGGs, the satellite galaxies in our sample occupy the lower part of the M_* range (middle panel of Figure 11) but the upper part of the M_{halo} range (right panel of Figure 11). Since the fraction of rising dispersion profiles decreases with M_* and increases with M_{halo} for the galaxies in our study as a whole, these two factors may have largely cancelled each other to result in a comparable average γ_{outer} and rising fraction for satellites and BGGs, but a larger spread in γ_{outer} for satellites. Our

sample size is not sufficient to probe further the statistics of γ_{outer} for these three types of galaxies. Future larger surveys can provide important new insights by comparing the kinematics of BGGs, satellites, and isolated galaxies at *fixed* M_* and M_{halo} .

We find a positive correlation between the outer σ gradient γ_{outer} and the gradient of the LOSVD kurtosis $\Delta h_4/\Delta \log R$ (Figure 6). Based in part on this correlation, we argue that the rising σ profiles seen in our galaxies and the trends with M_* and M_{halo} are likely caused at least in part by variations in total mass profiles (including variations from isothermal). It is unlikely that rising σ profiles can be explained by tangential velocity anisotropy alone, but a positive gradient in circular velocity is consistent with both positive σ gradients and positive h_4 gradients. Our results can accommodate a range of velocity anisotropy, so long as any tangential anisotropy (associated with negative h_4) is not extreme enough to overcome gradients in circular velocity (associated with positive h_4) as the primary influence on $\langle h_4 \rangle$, which we find to be generally positive.

Most likely, both mass profile shape and velocity anisotropy play a role in determining the σ profile. More detailed modeling is required to make any definitive statements, but the correlations with galaxy mass and M_{halo} suggest at least one possible scenario. Figure 9 shows an apparently sharp cutoff of the maximum allowed γ_{outer} that increases with M_{halo} . Perhaps this is because M_{halo} controls the underlying total mass profile shape (in central galaxies) and the presence of non-equilibrium motions (in satellites moving with respect to the cluster), with the mass of the halo dictating the maximum possible rise of outer $\sigma(R)$. Figure 7 shows a similar cutoff for the *minimum* allowed γ_{outer} , which increases with M_K . Perhaps this is because substantial radial anisotropy, likely needed to explain very steeply falling σ , cannot survive the extensive merger histories typical of very massive galaxies. At the most extreme masses nearly every galaxy may converge on a homologous anisotropy profile - not necessarily isotropic, but with less extreme radial anisotropy at large radii - while lower mass galaxies show a range of anisotropy profiles. This scenario is consistent with the fact that our observed h_4 implies some variation in mass profiles and can accommodate a range of anisotropy. It is also consistent with how the classification of “flat” profiles impacts the correlations, with f_{rising} correlating more strongly than f_{falling} with M_{halo} , while f_{falling} correlates more strongly than f_{rising} with M_* .

This scenario is again speculative, based on qualitative arguments about the connections among enclosed mass, σ , velocity anisotropy, and h_4 that have been noted in the literature. Our ongoing dynamical modeling efforts using the reported kinematics will provide deeper insights into the trends reported in this paper.

ACKNOWLEDGEMENTS

We thank Marijn Franx for useful discussions. The MASSIVE survey is supported in part by NSF AST-1411945, NSF AST-1411642, HST-GO-14210, and HST-AR-1457.

REFERENCES

- Alabi A. B., et al., 2016, *MNRAS*, **460**, 3838
 Arnold J. A., et al., 2014, *ApJ*, **791**, 80
 Auger M. W., Treu T., Bolton A. S., Gavazzi R., Koopmans L. V. E., Marshall P. J., Bundy K., Moustakas L. A., 2009, *ApJ*, **705**, 1099
 Auger M. W., Treu T., Bolton A. S., Gavazzi R., Koopmans L. V. E., Marshall P. J., Moustakas L. A., Burles S., 2010, *ApJ*, **724**, 511
 Baes M., Dejonghe H., Buyle P., 2005, *A&A*, **432**, 411
 Bender R., Kormendy J., Cornell M. E., Fisher D. B., 2015, *ApJ*, **807**, 56
 Binney J., Mamon G. A., 1982, *MNRAS*, **200**, 361
 Bonfanti P., Rampazzo R., Combes F., Prugniel P., Sulentic J. W., 1995, *A&A*, **297**, 28
 Brodie J. P., et al., 2014, *ApJ*, **796**, 52
 Brough S., Proctor R., Forbes D. A., Couch W. J., Collins C. A., Burke D. J., Mann R. G., 2007, *MNRAS*, **378**, 1507
 Cappellari M., 2013, *ApJ*, **778**, L2
 Cappellari M., Emsellem E., 2004, *PASP*, **116**, 138
 Cappellari M., et al., 2015, *ApJ*, **804**, L21
 Carrick J., Turnbull S. J., Lavaux G., Hudson M. J., 2015, *MNRAS*, **450**, 317
 Carter D., Efstathiou G., Ellis R. S., Inglis I., Godwin J., 1981, *MNRAS*, **195**, 15P
 Carter D., Inglis I., Ellis R. S., Efstathiou G., Godwin J. G., 1985, *MNRAS*, **212**, 471
 Carter D., Bridges T. J., Hau G. K. T., 1999, *MNRAS*, **307**, 131
 Cohen J. G., Ryzhov A., 1997, *ApJ*, **486**, 230
 Côté P., et al., 2001, *ApJ*, **559**, 828
 Cretton N., Rix H.-W., de Zeeuw P. T., 2000, *ApJ*, **536**, 319
 Crook A. C., Huchra J. P., Martimbeau N., Masters K. L., Jarrett T., Macri L. M., 2007, *ApJ*, **655**, 790
 Crook A. C., Huchra J. P., Martimbeau N., Masters K. L., Jarrett T., Macri L. M., 2008, *ApJ*, **685**, 1320
 Davies R. L., Illingworth G., 1983, *ApJ*, **266**, 516
 Davies R. L., Illingworth G. D., 1986, *ApJ*, **302**, 234
 Davis T. A., Greene J., Ma C.-P., Pandya V., Blakeslee J. P., McConnell N., Thomas J., 2016, *MNRAS*, **455**, 214
 Deason A. J., Belokurov V., Evans N. W., McCarthy I. G., 2012, *ApJ*, **748**, 2
 Dejonghe H., Merritt D., 1992, *ApJ*, **391**, 531
 Dekel A., Stoehr F., Mamon G. A., Cox T. J., Novak G. S., Primack J. R., 2005, *Nature*, **437**, 707
 Dressler A., 1979, *ApJ*, **231**, 659
 Durrell P. R., et al., 2014, *ApJ*, **794**, 103
 Emsellem E., et al., 2011, *MNRAS*, **414**, 888
 Faber S. M., Burstein D., Dressler A., 1977, *AJ*, **82**, 941
 Falco M., Hansen S. H., Wojtak R., Brinckmann T., Lindholmer M., Pandolfi S., 2014, *MNRAS*, **442**, 1887
 Ferrarese L., et al., 2012, *ApJS*, **200**, 4
 Fisher D., Illingworth G., Franx M., 1995, *ApJ*, **438**, 539
 Foster C., et al., 2016, *MNRAS*, **457**, 147
 Franx M., Illingworth G., Heckman T., 1989, *ApJ*, **344**, 613
 Gerhard O. E., 1993, *MNRAS*, **265**, 213
 Gerhard O., Jeske G., Saglia R. P., Bender R., 1998, *MNRAS*, **295**, 197
 Gerhard O., Kronawitter A., Saglia R. P., Bender R., 2001, *AJ*, **121**, 1936
 Goulding A. D., et al., 2016, *ApJ*, **826**, 167
 Greene J. E., Janish R., Ma C.-P., McConnell N. J., Blakeslee J. P., Thomas J., Murphy J. D., 2015, *ApJ*, **807**, 11
 Hau G. K. T., Hilker M., Bridges T., Carter D., Dejonghe H., de Rijcke S., Quintana H., 2004, in Diaferio A., ed., *IAU Colloq. 195: Outskirts of Galaxy Clusters: Intense Life in the Suburbs*. pp 491–495, doi:10.1017/S1743921304001061
 Heisler J., Tremaine S., Bahcall J. N., 1985, *ApJ*, **298**, 8

- Hill G. J., et al., 2008, in Society of Photo-Optical Instrumentation Engineers (SPIE) Conference Series. , doi:10.1117/12.790235
- Huchra J., et al., 2005a, in Colless M., Staveley-Smith L., Stathakis R. A., eds, IAU Symposium Vol. 216, Maps of the Cosmos. p. 170
- Huchra J., et al., 2005b, in Fairall A. P., Woudt P. A., eds, Astronomical Society of the Pacific Conference Series Vol. 329, Nearby Large-Scale Structures and the Zone of Avoidance. p. Fairall
- Jarrett T. H., Chester T., Cutri R., Schneider S., Skrutskie M., Huchra J. P., 2000, *AJ*, **119**, 2498
- Kelson D. D., Zabludoff A. I., Williams K. A., Trager S. C., Mulchaey J. S., Bolte M., 2002, *ApJ*, **576**, 720
- Koopmans L. V. E., et al., 2009, *ApJ*, **703**, L51
- Kubo J. M., Stebbins A., Annis J., Dell’Antonio I. P., Lin H., Khiabani H., Frieman J. A., 2007, *ApJ*, **671**, 1466
- Lavaux G., Hudson M. J., 2011, *MNRAS*, **416**, 2840
- Loubser S. I., Sansom A. E., Sánchez-Blázquez P., Soechting I. K., Bromage G. E., 2008, *MNRAS*, **391**, 1009
- Ma C.-P., Greene J. E., McConnell N., Janish R., Blakeslee J. P., Thomas J., Murphy J. D., 2014, *ApJ*, **795**, 158
- Merritt D., Saha P., 1993, *ApJ*, **409**, 75
- Morganti L., Gerhard O., Coccato L., Martinez-Valpuesta I., Arnaboldi M., 2013, *MNRAS*, **431**, 3570
- Murphy J. D., Gebhardt K., Adams J. J., 2011, *ApJ*, **729**, 129
- Murphy J. D., Gebhardt K., Cradit M., 2014, *ApJ*, **785**, 143
- Napolitano N. R., et al., 2009, *MNRAS*, **393**, 329
- Newman A. B., Treu T., Ellis R. S., Sand D. J., Nipoti C., Richard J., Jullo E., 2013, *ApJ*, **765**, 24
- Newman A. B., Ellis R. S., Treu T., 2015, *ApJ*, **814**, 26
- Pandya V., et al., 2017, *ApJ*, **837**, 40
- Pota V., et al., 2015, *MNRAS*, **450**, 3345
- Raskutti S., Greene J. E., Murphy J. D., 2014, *ApJ*, **786**, 23
- Rines K., Geller M. J., Kurtz M. J., Diaferio A., 2003, *AJ*, **126**, 2152
- Romanowsky A. J., Douglas N. G., Arnaboldi M., Kuijken K., Merrifield M. R., Napolitano N. R., Capaccioli M., Freeman K. C., 2003, *Science*, **301**, 1696
- Rubin V. C., Ford Jr. W. K., Thonnard N., 1980, *ApJ*, **238**, 471
- Schauer A. T. P., Remus R.-S., Burkert A., Johansson P. H., 2014, *ApJ*, **783**, L32
- Schindler S., Binggeli B., Böhringer H., 1999, *A&A*, **343**, 420
- Sembach K. R., Tonry J. L., 1996, *AJ*, **112**, 797
- Simien F., Prugniel P., 1997, *A&AS*, **126**
- Simien F., Prugniel P., 1998, *A&AS*, **131**, 287
- Simien F., Prugniel P., 2000, *A&AS*, **145**, 263
- Skrutskie M. F., et al., 2006, *AJ*, **131**, 1163
- Sonnenfeld A., Treu T., Gavazzi R., Suyu S. H., Marshall P. J., Auger M. W., Nipoti C., 2013, *ApJ*, **777**, 98
- Thomas J., et al., 2007, *MNRAS*, **382**, 657
- Thomas J., et al., 2011, *MNRAS*, **415**, 545
- Thomas J., Saglia R. P., Bender R., Erwin P., Fabricius M., 2014, *ApJ*, **782**, 39
- Thomas J., Ma C.-P., McConnell N. J., Greene J. E., Blakeslee J. P., Janish R., 2016, *Nature*, **532**, 340
- Tonry J. L., 1985, *AJ*, **90**, 2431
- Treu T., Koopmans L. V., Bolton A. S., Burles S., Moustakas L. A., 2006, *ApJ*, **640**, 662
- Veale M., et al., 2017a, *MNRAS*, **464**, 356
- Veale M., Ma C.-P., Greene J. E., Thomas J., Blakeslee J., McConnell N., Walsh J., Ito J., 2017b, preprint, (arXiv:1703.08573)
- Ventimiglia G., Gerhard O., Arnaboldi M., Coccato L., 2010, *A&A*, **520**, L9
- Verolme E. K., et al., 2002, *MNRAS*, **335**, 517
- Wilkinson A., Sharples R. M., Fosbury R. A. E., Wallace P. T., 1986, *MNRAS*, **218**, 297
- Wu X., Tremaine S., 2006, *ApJ*, **643**, 210
- Wu X., Gerhard O., Naab T., Oser L., Martinez-Valpuesta I., Hilz M., Churazov E., Lyskova N., 2014, *MNRAS*, **438**, 2701
- van de Sande J., et al., 2017, *ApJ*, **835**, 104

APPENDIX A: INDIVIDUAL PROFILES

Each galaxy in our sample is fit to Equation 1 as described in Veale et al. (2017a). If the broken power law fit does not improve the χ^2 per degree of freedom (χ^2/DOF) by at least 0.3 over the single power law fit ($\gamma_1 = \gamma_2$), we use the single power law fit. We also do not allow best-fit profiles with $\gamma_2 < \gamma_1$, even if the χ^2/DOF is nominally improved by at least 0.3; most such fits barely meet that criterion, and by eye are not substantially different from galaxies fit by the single power law. Five additional galaxies that nominally require broken power law fits (with $\gamma_2 > \gamma_1$) according to the above criteria are reclassified to use the single power law fit, due to poor data quality or unusual σ profile shapes making the fit untrustworthy. These are NGC 0545, NGC 1272, UGC 01332, NGC 3862, and NGC 4839.

Figure A1 through Figure A6 show the σ profiles for all 85 galaxies (in the same order as Table 1), with the best-fit overlaid in red (with galaxies requiring broken power law fits using dashed lines). Individual bins with error bars on σ are shown, with the point shaded according to whether the bin is close to the positive major axis (black), minor axis (gray), or negative major axis (white). Note that “positive” and “negative” major axis are chosen arbitrarily, not to correspond to the red or blue shifted side in rotating galaxies.

Fits for a few galaxies were complicated by apparent errors in the radial coordinates of the bins. While the outer profiles are not affected by small errors in radius, the inner part of the profile fit can be substantially impacted by a small shift in radius. In most of these cases, a central bin placed unusually close to $R = 0$ would disrupt the fit by requiring a nearly flat γ_1 regardless of the shape of the rest of the profile, due to the much smaller σ errors in the centre. For these cases we re-fit the profile using orthogonal distance regression instead of the simple least-squares minimization used for the other fits, adding an error on R of 2.0 arcsec to all bins. This is indicated in Figure A1 through Figure A6 by showing the central bin in red, with a horizontal error bar. The following galaxies were re-fit in this way: NGC 0499, IC 0310, NGC 1684, NGC 1700, NGC 6223, NGC 6482, NGC 7550, and NGC 7626.

After these adjustments, the resulting fits to each galaxy achieve a reasonable representation of the overall rise or fall of σ in each profile. The single and double power law fits are not physically motivated, and are certainly not appropriate for extrapolating beyond the radial range of our data, whether out to large R or towards the galaxy centre. We do not attempt to capture more complicated features even in galaxies with better data quality, instead choosing to be as uniform as possible across our entire sample.

This paper has been typeset from a \LaTeX file prepared by the author.

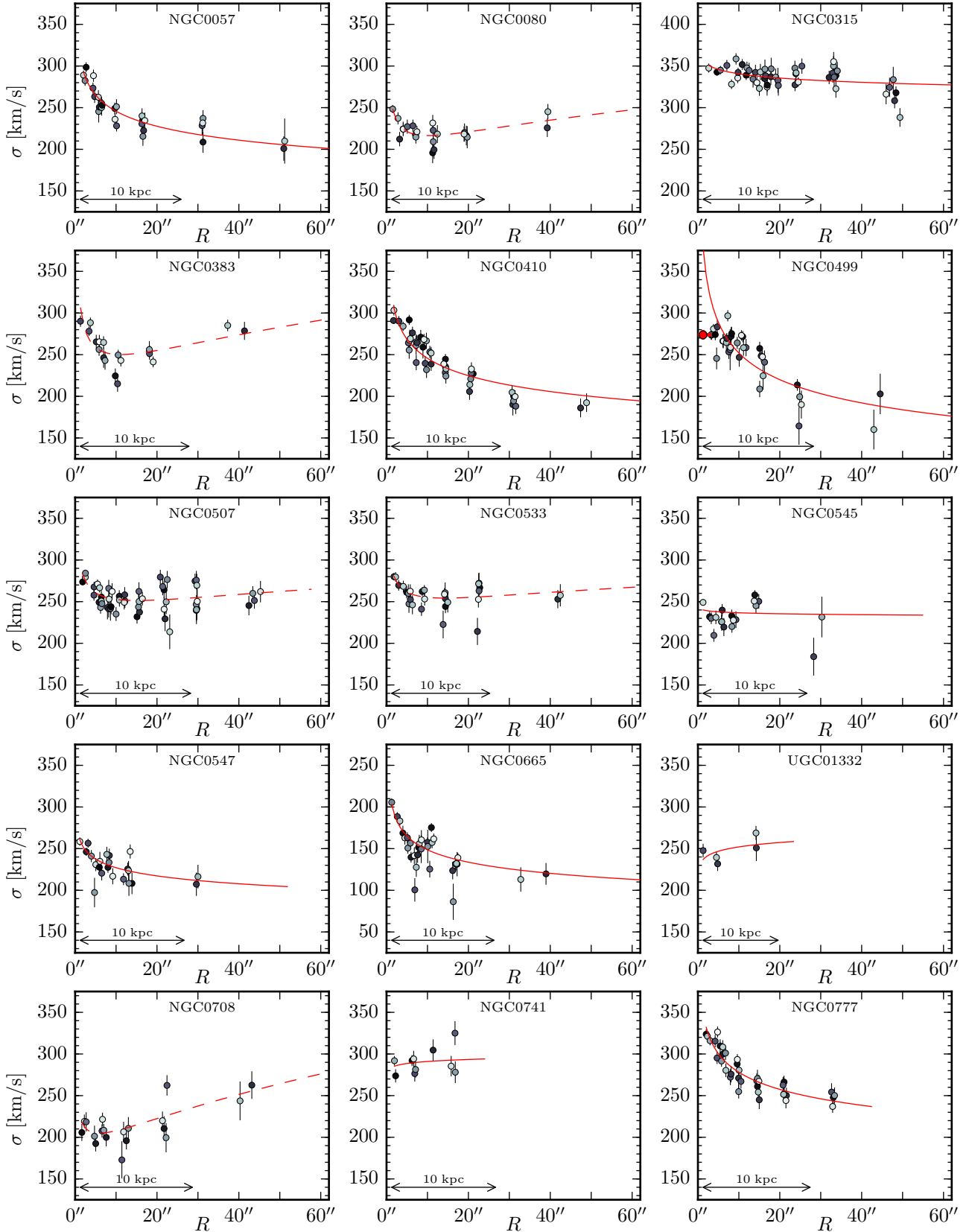


Figure A1. Individual galaxy dispersion profiles. Within each galaxy, σ for each spatial bin is shown with error bars, with point color corresponding to angle from major axis; black and white correspond to positive and negative major axis, and gray corresponds to the minor axis. Single (solid) and double (dashed) power law fits are shown in red. If the center bin is shown in red, with a horizontal error, the galaxy was re-fit with a 2.0 arcsec error bar in R (on all bins) to prevent misplaced central bins from disrupting the fit.

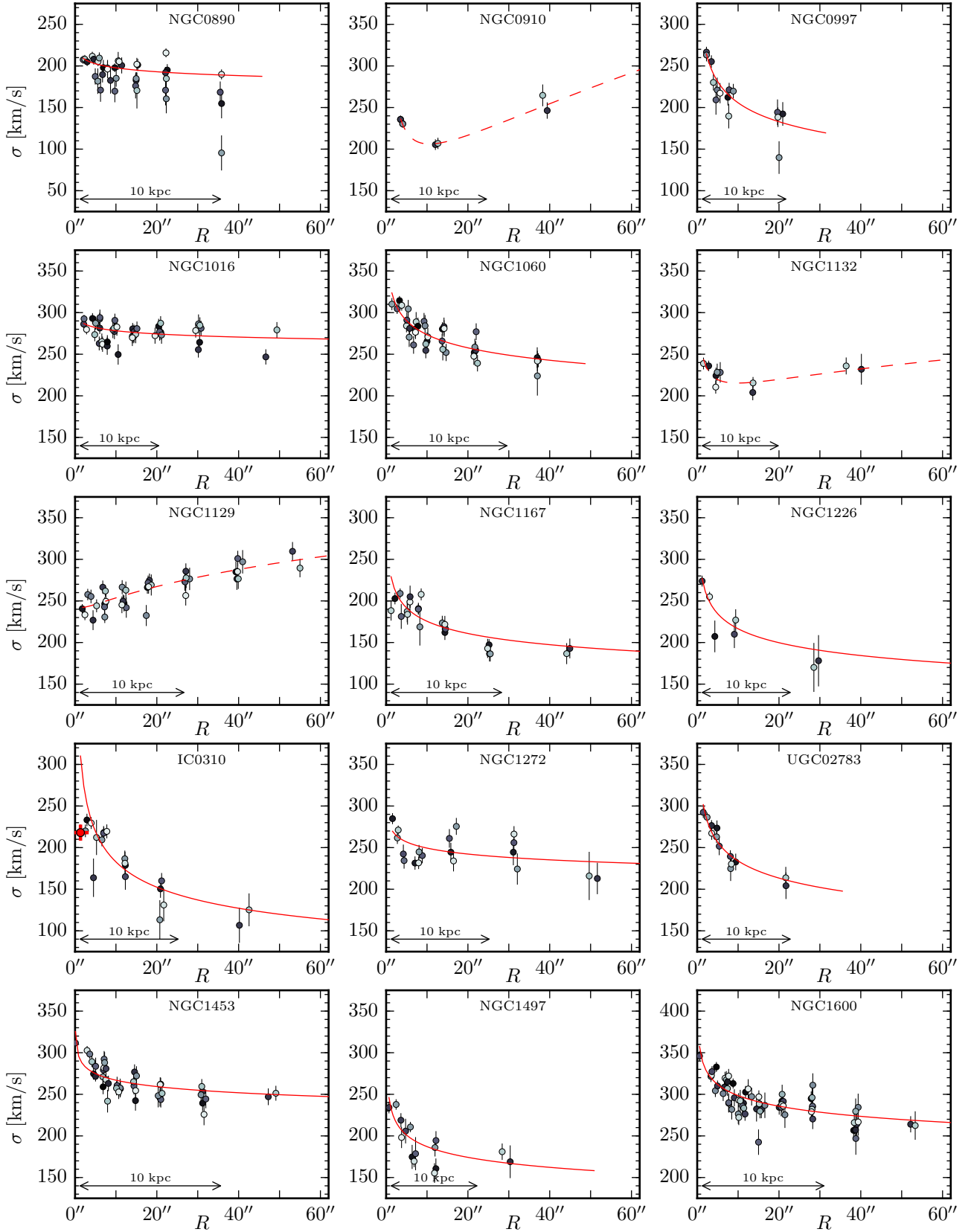


Figure A2. See Figure A1 for detailed caption.

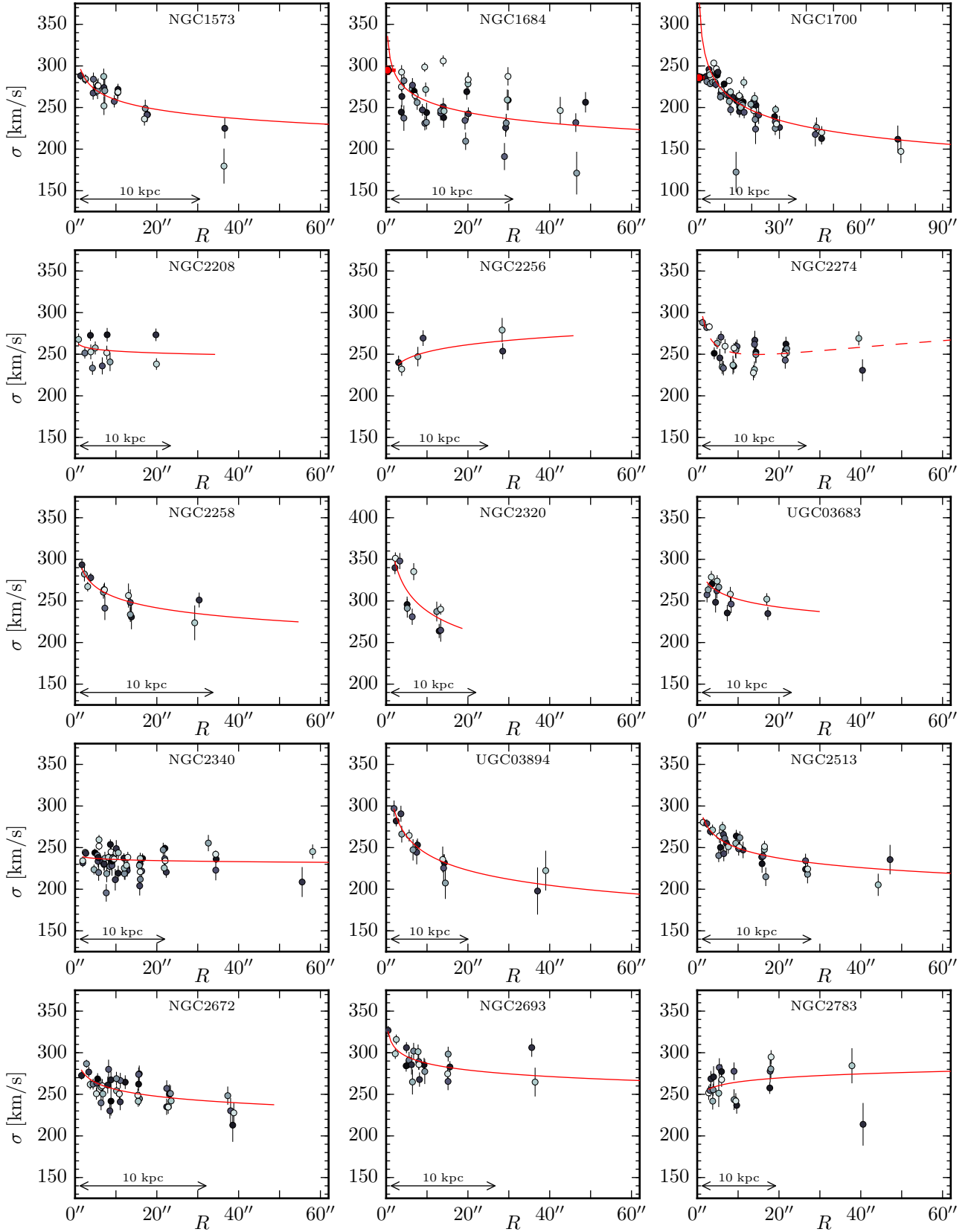


Figure A3. See Figure A1 for detailed caption.

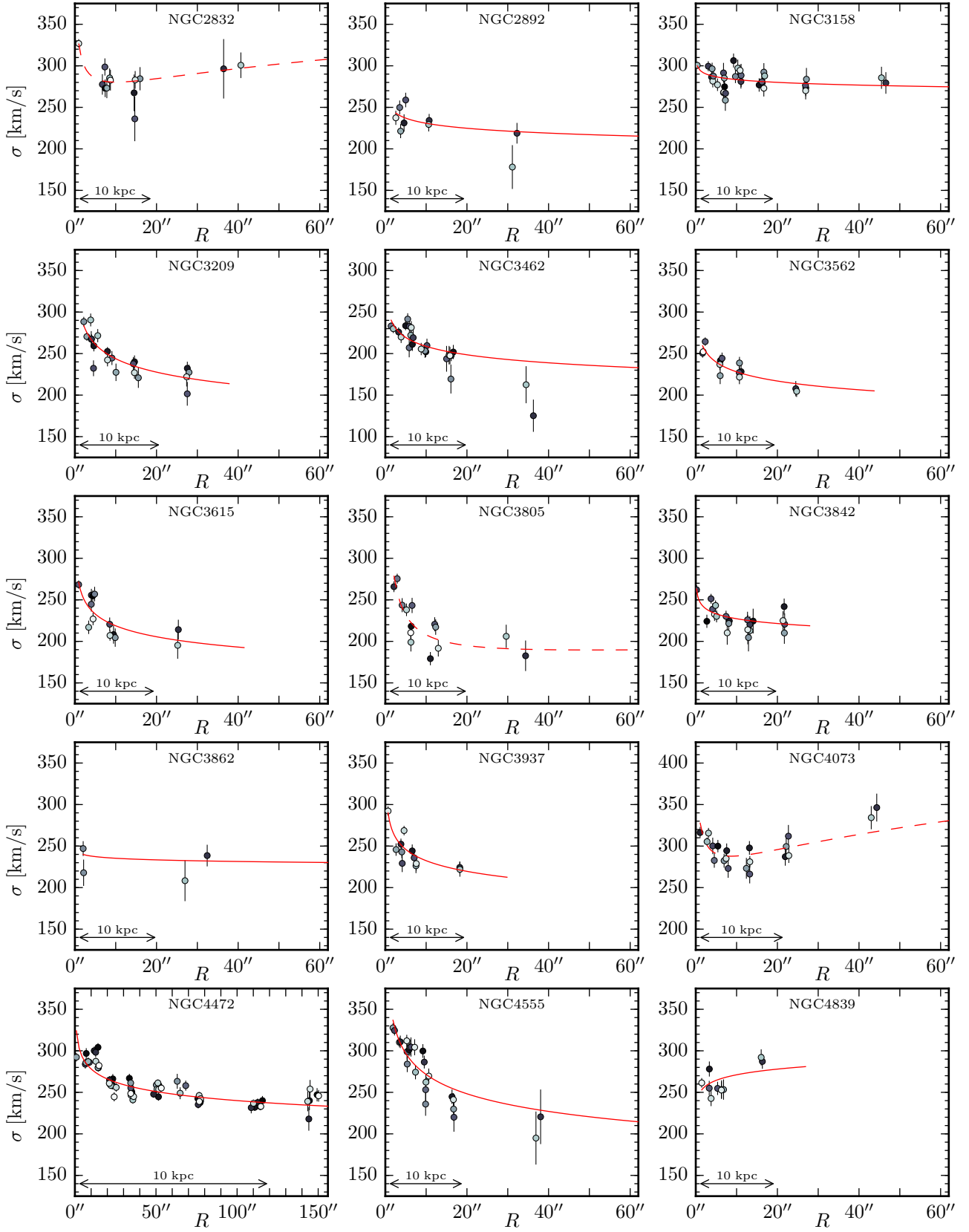


Figure A4. See Figure A1 for detailed caption.

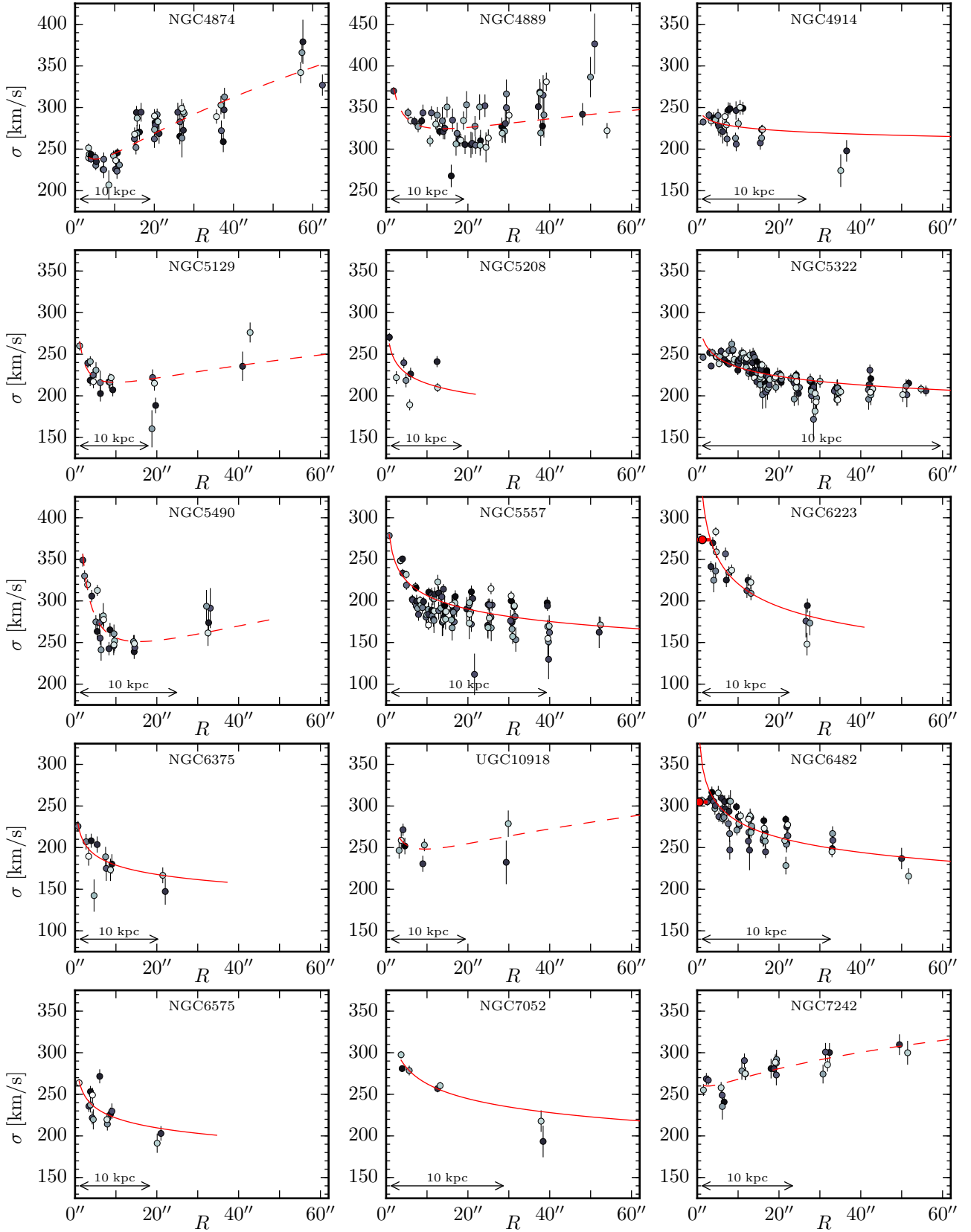


Figure A5. See Figure A1 for detailed caption.

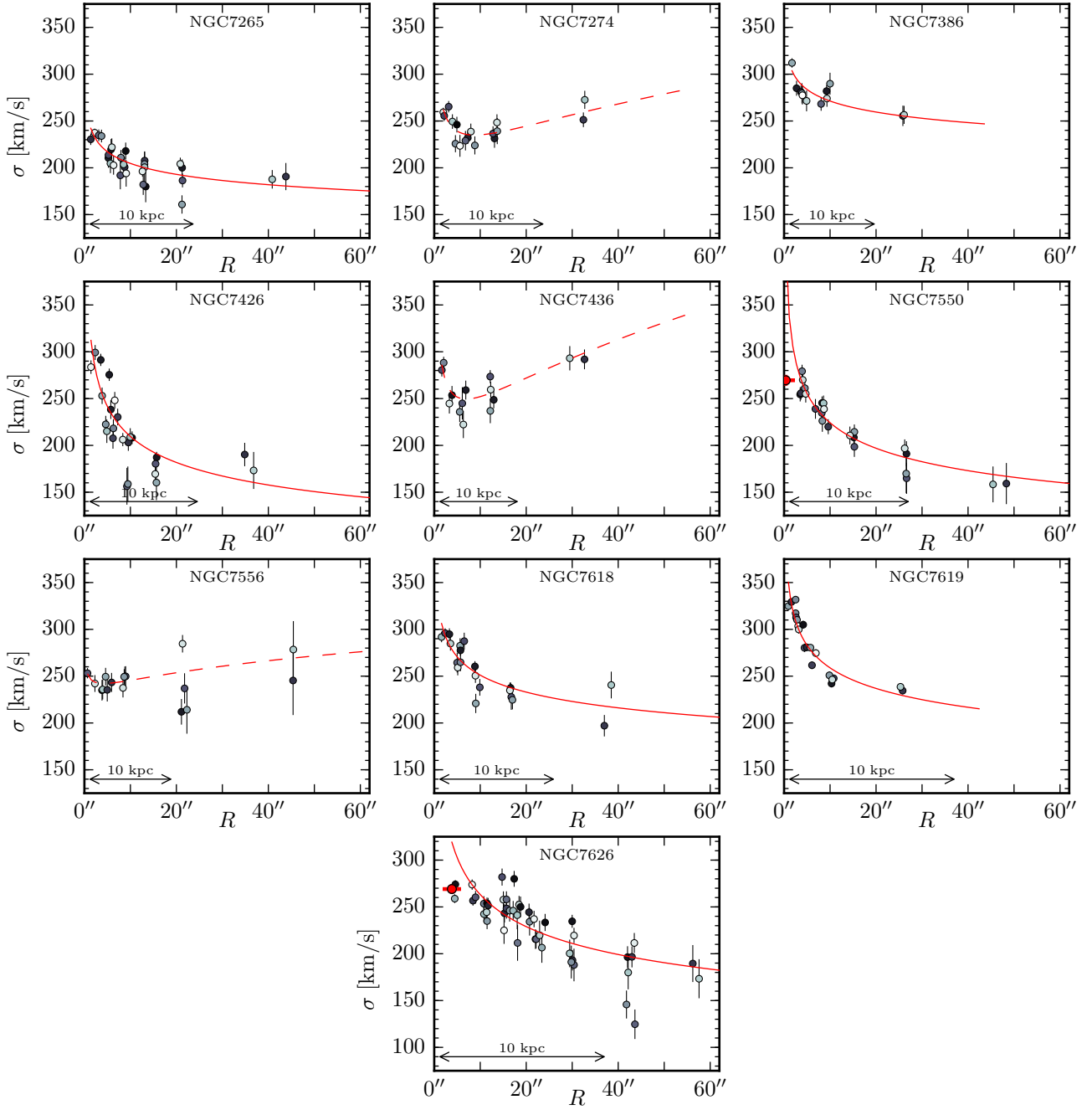


Figure A6. See [Figure A1](#) for detailed caption.